ktu
1922

KAUNAS UNIVERSITY OF TECHNOLOGY

MATHEMATICS AND NATURAL SCIENCES FACULTY

Nursultan Kainbayev

FORMATION AND RAMAN SPECTRA INVESTIGATION OF DOPED CERIUM OXIDE THIN FILMS FORMED USING E-BEAM DEPOSITION TECHNIQUE

Final project of Master degree

Supervisor
Prof. dr. Giedrius Laukaitis

KAUNAS, 2017

KAUNAS UNIVERSITY OF TECHNOLOGY
MATHEMATICS AND NATURAL SCIENCES FACULTY

FORMATION AND RAMAN SPECTRA INVESTIGATION OF DOPED CERIUM OXIDE THIN FILMS FORMED USING E-BEAM DEPOSITION TECHNIQUE

Final project of Master degree
Applied Physics (code 612F30005)

Supervisor
(signature) Prof. dr. Giedrius Laukaitis
(date)

Reviewer
(signature) Prof. dr. Liutauras Marcinauskas
(date)

Project made by
(signature) Nursultan Kainbayev
(date)

KAUNAS, 2017

KAUNAS UNIVERSITY OF TECHNOLOGY

Faculty of Mathematics and Natural Sciences
(Faculty)

Nursultan Kainbayev

(Student's name, surname)

Applied Physics (621F30005)

(Title and code of study programme)

" Formation and raman spectra investigation of doped cerium oxide thin films formed using

e-beam depositing technique "

DECLARATION OF ACADEMIC HONESTY

| 30 | May | 2017 |

Kaunas

I confirm that a final project by me, Nursultan Kainbayev, on the subject " Formation and Raman spectra investigation of doped cerium oxide thin films formed using e-beam depositing technique " is written completely by myself; all provided data and research results are correct and obtained honestly. None of the parts of this thesis have been plagiarized from any printed or Internet sources, all direct and indirect quotations from other resources are indicated in literature references. No monetary amounts not provided for by law have been paid to anyone for this thesis.

I understand that in case of a resurfaced fact of dishonesty penalties will be applied to me according to the procedure effective at Kaunas University of Technology.

_____   _____

(name and surname filled in by hand)   *(signature)*

CONTENTS

LIST OF ABBREVIATIONS AND MARKS

1. SOFC- solid oxide fuel cells
2. YSZ- yttrium-stabilized zirconia
3. GDC- cerium oxide doped with gadolinium
4. SDC- cerium oxide doped with samarium
5. REE- rare-earth elements
6. PEFC- polymer electrolyte fuel cells
7. PEM- proton exchange membrane
8. KOH- potassium hydroxide
9. GDL- gas diffusion layer
10. MEU- membrane-electrode unit
11. PEM- polymer electrolyte membrane
12. YDC -cerium oxide doped with yttrium
13. CDC - cerium doped with calcium
14. LSGM- lanthanum gallate ceramic that include lanthanum strontium gallium magnesium
15. BYO- bismuth yttrium oxide
16. BCN- barium cerate
17. SYC- strontium cerate
18. LSF- lanthanum strontium ferrite
19. LSC- lanthanum strontium cobaltite
20. LSCF- lanthanum strontium cobaltite ferrite
21. LSMF- lanthanum strontium manganite ferrite
22. SSC- samarium strontium cobaltite
23. LCCF- lanthanum calcium cobaltite ferrit
24. PSM- praseodymium strontium manganite
25. PSMF- praseodymium strontium manganite ferrite
26. PVD – physical vapor deposition
27. XRD- X-ray diffraction
28. SEM- scanning electron microscope
29. EDS- electron dispersive spectroscopy
30. FFSl -film-forming solution
31. FFSb - film-forming substance

32. ES- evaporated substance
33. RF- radio frequency
34. HTSC- high-temperature superconductors
35. HF- high-frequency
36. TPB - three-phase boundaries
37. ODV- oxygen defects of vacancies
38. FWHM- full width half maximum

LIST OF FIGURE CAPTIONS

LIST OF TABLE CAPTIONS

Kainbayev, N. Formation and Raman spectra investigation of doped cerium oxide thin films formed using e-beam depositing technique. Final project of *master degree* / supervisor Prof. dr. Giedrius Laukaitis. Kaunas University of Technology, Mathematics and Natural Sciences faculty, department of physics.

Kaunas, 2017. 69 p.

SUMMARY

The investigation of new functional materials (ceramics) based on cerium (IV) oxides is a promising field of scientific research. A wide application in the industry received composite materials based on CeO_2–Gd_2O_3 and CeO_2–Sm_2O_3.

In this work thin films were formed on the basis of (CeO_2 with 10 mol% Gd_2O_3 (GDC10), CeO_2 with 20 mol% Gd_2O_3 (GDC20), CeO_2 with 15 mol% Sm_2O_3 (SDC15), CeO_2 with 20 mol% Sm_2O_3 (SDC20)) using e-beam technique in this work. The deposition rate and temperature of the substrate had influence on the formed doped cerium oxide (SDC and GDC) thin films properties. Sm and Gd doped cerium oxide thin films (~1.9 μm) were deposited on SiO_2, Alloy 600 (Fe-Ni-Cr), Si(111), Si (100) and Al_2O_3 substrates. Investigations of the formed thin films were carried out using a Scanning electron microscope (SEM), Electron dispersive spectroscopy (EDS), X-ray diffraction (XRD), and Raman spectroscopy.

It has been established that the cerium oxide based ceramic retains the crystalline structure, regardless of the concentration of the dopant and used substrate type. The most dominant crystallographic orientation of formed thin films was cubic (111). Raman spectroscopy measurements showed the peak ($465cm^{-1}$) of pure ceria corresponding to F2g vibrational mode. First-order peaks, inherent to cerium oxide, were shifted to a region of lower wavenumbers and depend on dopant concentration. The peaks for all formed thin films were similar to each other in form but the position, half width and their intensity varied depending on the dopant concentration. Raman peaks position at $550 \ cm^{-1}$ and $600 \ cm^{-1}$ could be explained as change of oxygen vacancy amount due to the cerium transition between oxidized and reduced forms of $Ce^{3+} \rightleftarrows Ce^{4+}$.

Kainbayev, N. Plonų cerio oksido su priemaišomis sluoksnių formavimas garinant elektronų spinduliu ir tyrimas Ramano spektroskopija. Magistro baigiamasis projektas \ vadovas prof. dr. Giedrius Laukaitis. Kauno technologijos universiteto Matematikos ir gamtos mokslų fakultetas.

Kaunas, 2017. 69 psl.

SANTRAUKA

Cerio (IV) oksido funkcinių keramikų tyrimai yra perspektyvi tyrimų sritis. Pramonėje plačiai naudojamos CeO_2–Gd_2O_3 ir CeO_2–Sm_2O_3 kompozicinės medžiagos.

Šiame darbe plonos CeO_2 su 10 mol% Gd_2O_3 (GDC10), CeO_2 su 20 mol% Gd_2O_3 (GDC20), CeO_2 su 15 mol% Sm_2O_3 (SDC15), CeO_2 su 20 mol% Sm_2O_3 (SDC20) dangos buvo suformuotos naudojant garinimą elektronų spinduliu. Naudojant šį metodą, nusodinimo greitis ir padėklo temperatūra įtakojo suformuotų legiruoto cerio oksido plonų dangų savybes. Legiruotos (Sm ir Gd) plonos cerio oksido plonos dangos (~ 1,9 μm) buvo užneštos ant SiO_2, Alloy 600 (Fe-Ni-Cr), Si (111), Si (100) ir Al_2O_3 padėklų. Suformuotų plonų dangų tyrimai buvo atlikti skenuojančiu elektroniniu mikroskopu (SEM), elektronų dispersinės spektroskopijos (EDS), Rentgeno spindulių difrakcijos (XRD) metodais ir Ramano spektroskopijos metodu.

Darbe buvo nustatyta, kad suformuoti ploni GDC bei SDC sluoksniai turi kristalinę struktūrą, nepriklausomai nuo priemaišų kiekio ir naudojamo padėklo. Dominuojanti kristalografinė orientacija buvo kubinė (111). Naudojant Ramano spektroskopiją buvo nustatyta gryno cerio smailė (465cm^{-1}) atitinkanti F2g vibracinį lygmenį. Būdingos pirmos eilės cerio oksido smailės, keičiant priemaišų koncentraciją, pasislenka į mažesnių bangos skaičių sritį. Visų suformuotų GDC bei SDC plonų sluoksnių Ramano smailės buvo panašios viena į kitą savo forma. Tiriamos dangos sudėties sąlygojo smailių padėtį, jų pusplotį bei intensyvumą. Tyrimuose nustatytos 550 cm^{-1} ir 600 cm^{-1} smailių padėtys paaiškina deguonies vakansijų skaičiaus kitimą dėl cerio valentingumo pokyčio, t.y. $Ce^{3+} \rightleftarrows Ce^{4+}$.

INTRODUCTION

The creation of new functional materials based on oxides (catalysts, counter electrodes of electrochromic devices, solid oxide fuel cells), including cerium (IV) oxide, is a promising field of scientific research corresponding to priority areas of Lithuania's scientific and technological development "Technologies for the production and processing of functional nanomaterials". The composite materials CeO_2–Gd_2O_3 and CeO_2–Sm_2O_3 were widely used in industry because of the ease of cerium transition between the oxidized and reduced forms of $Ce^{3+} \rightleftarrows Ce^{4+}$[2, 5]. Gd (IV) and Sm (IV) oxides influence this equilibrium, and also increase the thermal stability and transmittance in the visible region of the ceria (IV) oxide spectrum.

The known physical and chemical, combined methods for the production of oxide CeO2-CeO_2–Gd_2O_3 and CeO_2–Sm_2O_3 in thin-film states are mainly energy-intensive and require the use of expensive equipment. In our case, we have chosen the method of electron beam evaporation (E-beam deposition). In the method of electron beam evaporation, changes in the deposition rate, pressure and temperature of the substrate affect the properties of oxide films. By changing the application parameters, we can obtain thin films with a homogeneous structure and a homogeneous shape without any defects and cracks [1, 2, 5].

A fuel cell is a device that converts chemical energy into electrical energy. There are different types of fuel cells designed for a specific application, the most important difference between them is the kind of electrolyte they use. This study was carried out using a solid oxide electrolyte, which is a cerium oxide with (Gd_2O_3 and Sm_2O_3) dopant.

The properties of a thin film electrolyte in many respects define operational characteristics of the fuel cell. High ionic conductivity, mechanical strength thermal resistance and gas tightness are the main requirements to the electrolyte ensure stable and long term operation of fuel cells with high electrical performance, preventing the loss of fuel [5].

The purpose of the research is to form a thin film on the basis of cerium oxide (CeO_2) with dopants Sm and Gd using e-beam evaporation technique, to investigate the microstructure and Raman spectra study are the purpose of the research.

The early theories, on the basis of which the search for an optimum dopant for CeO_2 was carried out, were generally based on consideration of deformation of a lattice in general and did not tale into account local microstructure of a solid electrolyte.

With development of new methods of the analysis there was an opportunity to find the additional parameters influencing the properties of solid solution which are not connected with technological features of their production.

The method of Raman spectroscopy enabled us to obtain additional information on oxygen vacancies in the investigated solid solutions.

The main tasks of the research:

1. To form a thin film on the basis of (CeO$_2$ with 10 mol% Gd$_2$O$_3$ (GDC10), CeO$_2$ with 20 mol% Gd$_2$O$_3$ (GDC20), CeO$_2$ with 15 mol% Sm$_2$O$_3$ (SDC15), CeO$_2$ with 20 mol% Sm$_2$O$_3$ (SDC20)) using e-beam technique in Alloy 600 (Fe-Ni-Cr), Si (111), Si (100) and Al$_2$O$_3$ substrates.
2. To investigate the microstructural properties with SEM, XRD, EDS.
3. To analyze of Raman spectra based on Gd and Sm doped ceria thin films.

1. LITERATURE REVIEW

This chapter describes the theory of cerium oxide and technical requirements for the production of thin films based on CeO_2 cerium oxide.

1.1. GENERAL BACKGROUND OF CERIUM OXIDE (CeO_2) AND CRYSTAL STRUCTURE

Cerium is a well-known rare-earth element. The element cerium was first extracted from the mineral called "tserit", by Jons Jakob Berzelius and Wilhelm Hisinger in Sweden. Cerium oxides are of great interest due to their unique properties in terms of various applications. CeO_X thin films have a lattice constant equal to 0.541 nm, eight equivalent oxygen anions surround each cerium ion, and each tetrahedral anion is coordinated by four cerium cations [1]. See the Fig. 1.1.1 and it differs a little from the lattice constant of silicon, which makes it possible to create epitaxial insulating layers in silicon technology. Thus, CeO_X films are well suited for applications in optical, electro-optic, microelectronic and optoelectronic devices. The valence of cerium affects the structure of cerium oxides: Cerium (IV) oxide CeO_2 forms a cubic lattice, whereas cerium (III) Ce_2O_3 oxides have a hexagonal crystal lattice. It was established that nanocrystalline CeO_X films mainly consist of grains of CeO_2, with a considerable concentration of Ce^{3+} observed at the grain boundaries, forming amorphous Ce_2O_3. A small amount of Ce^{3+} is also located around the vacancies of oxygen atoms [2]. It is apparent that physical properties of the film significantly depend on state of its surface, stoichiometry, crystallinity, density, microstructure and crystallographic orientation, that is, first of all, on methods of thin film manufacturing.
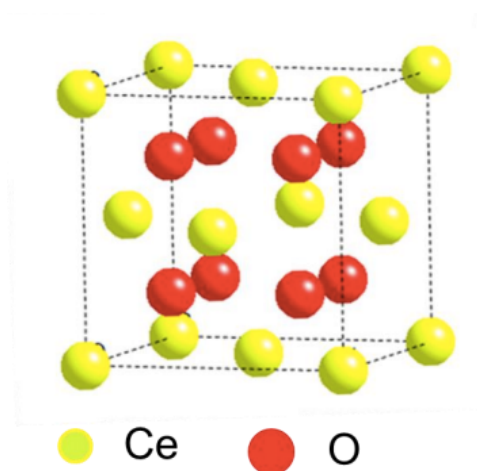
Fig. 1.1.1. Atomic configuration for the unit cell of fluorite-structured CeO_2 [1]

1.2. MORPHOLOGY AND NANOSTRUCTURE

Morphology plays a decisive role in the influence on the surface characteristics of materials. The crystal plane is one of the most widespread morphological characteristics considered in cerium oxide crystals. CeO_2 in the cubic fluorite structure has three planes with a low index: (100), (110) and (111). The planes (100) are unstable, but it is possible to stabilize them by defects or particles that compensate for the charge present, for example, in ligands or surfactants [3, 4]. The surfaces (110) are charged with neutral stoichiometric fractions of anions and cations in each plane, which leads to the absence of a dipole moment perpendicular to the surface. The surfaces (111) also do not have a dipole moment perpendicular to the surface. In contrast to the (110) planes, the surfaces (111) consist of a neutral three-plane repeating unit terminating in one plane of the anion [2, 3, 4].
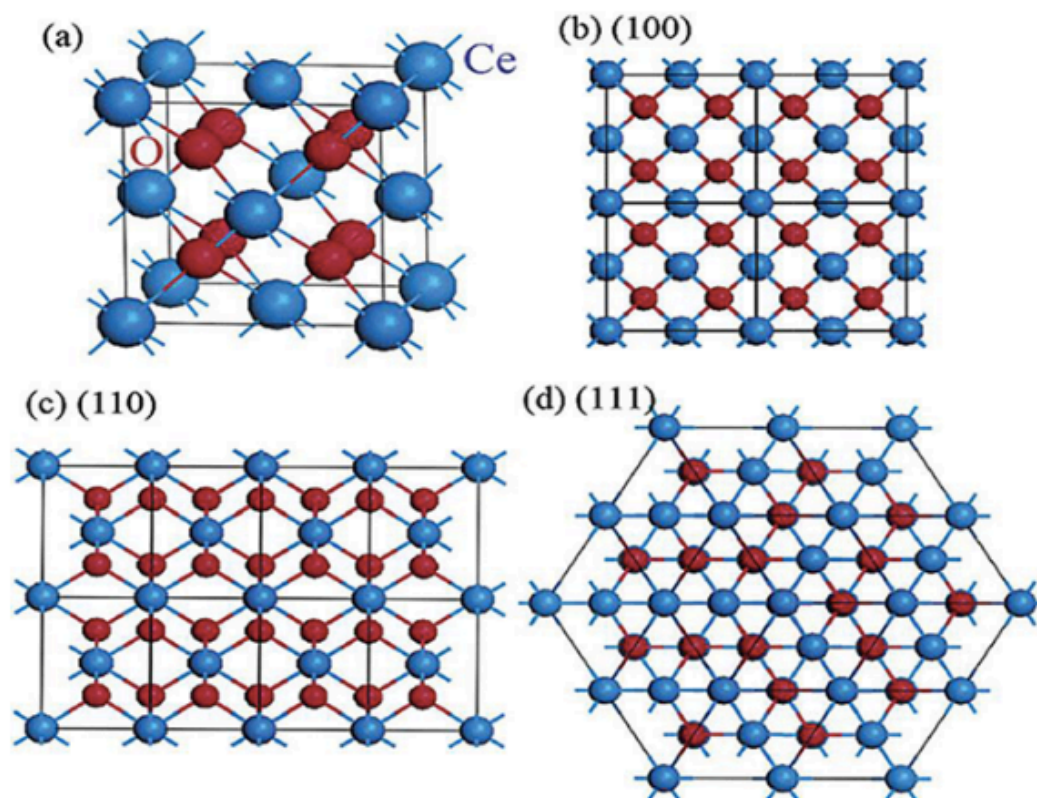
Fig. 1.2.1. The face-centred crystal cell of the CeO_2 structure: the (100), (110) and (111) planes of the CeO_2 structure [2]

As the particle size decreases for cerium oxide (CeO_2), the parameters of the elementary cells increase [5]. Table 1.2.1 shows the dependence of the values of the unit cell parameter on the particle size for the CeO_2.

Table 1.2.1. Dimensions and composition of CeO_2 nanoparticles [5].

Particle size, nm	The fraction of cerium atoms in the near-surface layer, % (calculated data)	$Ce^{3+}/(Ce^{3+}+ Ce^{4+})$, % (Experimental data)	Rated structure
7.0	27	21	$CeO_{1.894}$
4.6	43	38	$CeO_{1.810}$
2.6	75	74	$CeO_{1.630}$

The observed character of the change in the cell size is caused by a gradual decrease in the effective degree of cerium oxidation due to the removal of a part of the oxygen atoms on the surface of the particles from the corresponding crystallographic positions with the formation of oxygen vacancies.

1.3. OXYGEN VACANCY DEFECTS

Cerium oxide has a fluorite structure with Fm-3m space group. The intrinsic defects are caused by the alternative presence and absence of cerium cation in the eight coordination sites. The defects can also be formed by the reaction with a solid substance or atmosphere [5]. Three different types of internal/subsurface defects in ceria are Frenkel (cation) defect, anti-Frenkel (anion) defects, and Schottky defect. Frenkel (or interstitial) defect is formed when an atom or ion leaves its place in the lattice, it moves to an interstitial site close to its original location and a vacancy in the original site is formed. Schottky defects are formed when oppositely charged ions leave their lattice sites, create vacancy sites and these vacancies provide a total neutral charge of the ionic solid substance (Fig. 1.3.1) [5, 6]. In ceria, the energies of cation Frenkel defects (8.86 eV/per defect) and Schottky defects (3.33 eV) are higher than the energies of the Frenkel oxygen defects (2.81 eV). Therefore Frenkel-type oxygen defects must be the main form of intrinsic disorder [7].
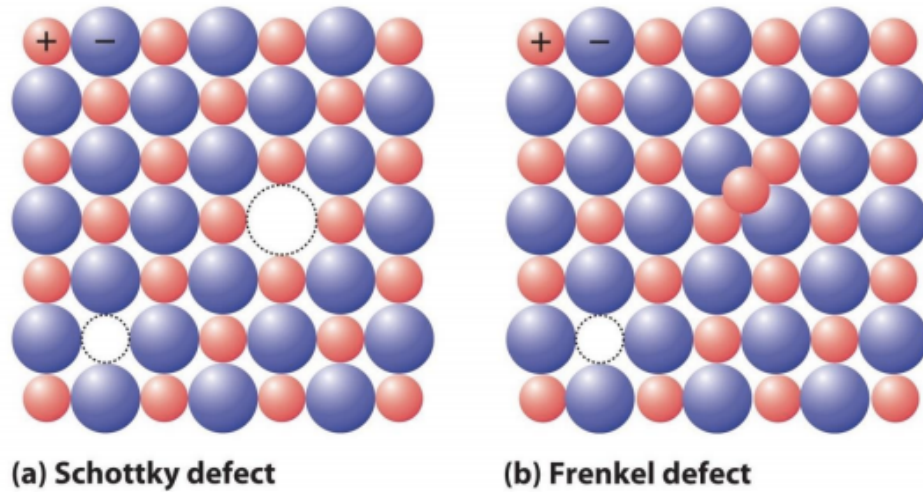
Fig. 1.3.1. Comparison of the lattice differences between the Schottky defect and the Frenkel defect [6]

Anion defects such as the Frenkel-type defects in oxygen lead to the formation of pairs of oxygen vacancies and oxygen atoms in the interstices. As a rule, these defects do not change the stoichiometric composition and usually have a low concentration. However, cerium oxide can form a high concentration of vacancy defects, removing oxygen ions in a reduced medium, which causes a change in the stoichiometry from CeO_2 to CeO_{2-x} ($0 < x < 0.5$). In this case, the new oxygen vacancies should compensate for the negative charges produced when oxygen is removed. After removal of oxygen from the CeO_2 lattice, the remaining electrons are associated with a change in the charge of two cerium atoms from +4 to +3. The process is illustrated by the following equation:

$$CeO_2 \ CeO_{2-x} + {}_{x/2} O_2 \ (g) \ (0 < x < 0.5) \qquad (1)$$
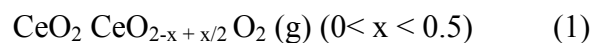
Oxygen defects of vacancies (ODV) of cerium oxide enable cerium oxide to act as an oxygen buffer for storing oxygen in a medium with a high oxygen content and to release oxygen into a medium with a low oxygen content. This unique property is associated with the exchange of oxidation states Ce^{4+} and Ce^{3+} in combination with ODVs formation. This property is also called an oxygen storage capacity, which positively correlates with the activity of catalysts/electrolytes in automobile emission control systems and solid oxide fuel cells [8, 9, 10].

1.4. CONDUCTIVITY OF CeO$_2$

Mobile oxygen vacancies are formed in its structure upon substitution of Ce^{4+} for a trivalent rare-earth element due to the dissolution of rare-earth oxides (Sm$_2$O$_3$, Gd$_2$O$_3$, Y$_2$O$_3$, etc.).

$$M_2O_3 \xrightarrow{CeO_2} 2M_2' + 3O_O^x + V_O^{**} \qquad (2)$$
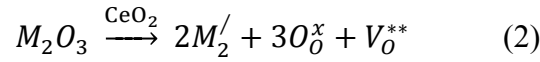
The dependence of ionic electrical conductivity of doped cerium oxide CeO$_2$ has an extreme character. The first portions of the admixture introduced into CeO$_2$, due to the increase in the concentration of oxygen vacancies, lead to an increase in the ionic conductivity (Fig. 1.4.1). At concentrations greater than x> 0.2, the electrical conductivity decreases, partially due to the formation of sedentary associates $(M_{Ce}' V_O^{**})^*$[11], partially as a result of the formation within the fluorite structure of microphases of the cubic structure (C-type), similar to the structure of the introduced impurity M$_2$O$_3$. For example, the oxide of the composition Ce$_{0.60}$ Gd$_{0.40}$ O$_{1.80}$ has a fluorite structure (F-type), and Ce$_{0.50}$ Gd$_{0.50}$ O$_{1.80}$ belongs to the C-type structure [11].
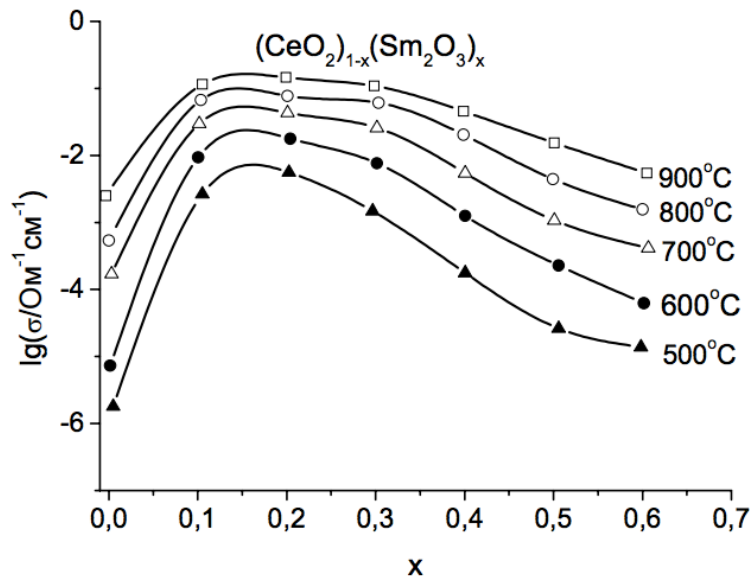
Fig. 1.4.1. Concentration dependencies of ionic conductivity of Cerium oxide doped with samarium (CeO$_2$) 1-x (Sm$_2$O$_3$) x at different temperatures [12]

Table 1.4.1 presents the values of the ionic conductivity of doped ceria. The electrolyte of composition Ce$_{0.9}$Gd$_{0.1}$O$_{1.95}$ has the highest ionic electrical conductivity.

Table 1.4.1. Ionic conductivity of CeO_2 - M_2O_3 systems in air [13].

M_2O_3	Content (mol%)	Ionic conductivity at 700° C ($10^{-2}\Omega^{-1}$ cm^{-1})	Ionic conductivity at 500°C ($10^{-2}\Omega^{-1}$ cm^{-1})	Activation energy (kJ/mol)
Sm_2O_3	10	3.45	0.29	68
Gd_2O_3	10	3.62	0.38	70
Y_2O_3	5	1.0	0.021	95
CaO	5	2.0	0.15	80

The use of doped cerium oxide as an electrolyte is associated with the appearance of an electronic conductivity component on the anode side at low partial oxygen pressures (the fuel part of the element) (Figs. 1.4.2 and 1.4.3). Fig. 1.4.2 shows the isotherms of electrical conductivity $Ce_{0.8}Sm_{0.2}O_{1.9-\delta}$ as a function of the partial pressure of oxygen in the gas phase. It is seen that at low pressures the contribution of electron conduction sharply increases.
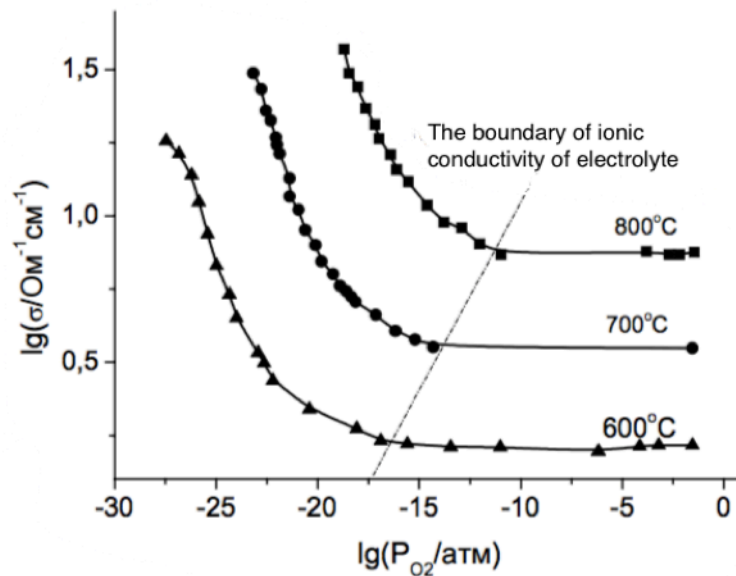
Fig. 1.4.2. Isothermal dependences of electrical conductivity $Ce_{0.8}Sm_{0.2}O_{1.9-\delta}$ on the partial pressure of oxygen in the gaseous phase [5]
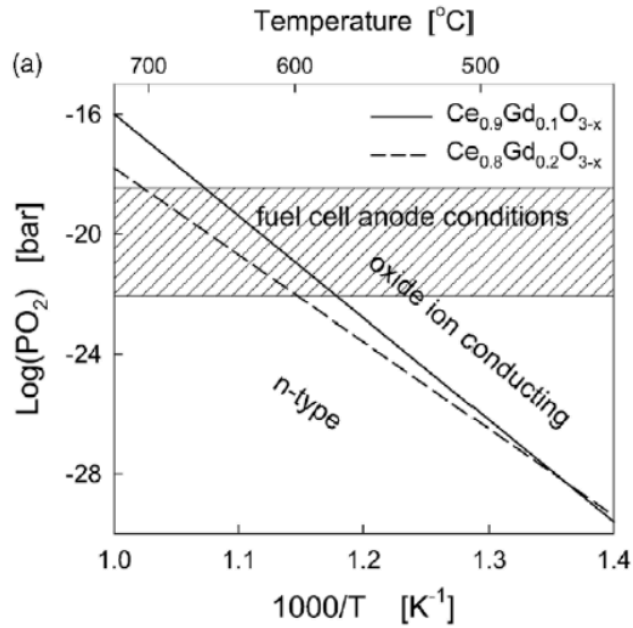
Fig. 1.4.3. The limits of the existence of pure ionic conductivity of electrolyte $Ce_{0.9}Gd_{0.1}O_{3-\delta}$ and $Ce_{0.8}Gd_{0.2}O_{3-\delta}$ depending on the oxygen pressure and temperature [14]

The appearance of the electron component of conductivity at low oxygen pressures is associated with the formation of excess oxygen vacancies.

$$2Ce_{Ce}^4 + 4O_O^\times = 3O_0^\times + V_O^{\cdot\cdot} + 2Ce_{Ce}^/ + \frac{1}{2}O_2 \qquad (3)$$
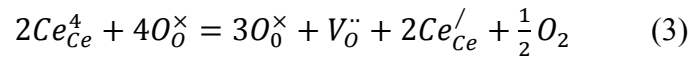
The effective positive charge of oxygen vacancies is compensated by the formation of electrons that are supposedly localized on cerium ions with the formation of bound Ce^{3+} ions participating in the charge transfer and causing a mixed conductivity of the electrolyte [12].

To conduct oxygen ions the material must have some defects [25]. The membrane usually consists of the layers of fluorite or perovskite arranged so that they have either vacancies or interstitial defects. This enables oxygen anions to move from vacancy to vacancy in the lattice, from the cathode to the anode. It was shown that the oxygen anion conductivity depends on the size of the crystal lattice [26].

YSZ exhibits purely oxygen ionic conduction (with no electronic conduction). Thus, oxide ions from the cathode jump from hole to hole until they reach the anode.

Other oxides on the base of ceramic electrolyte, which can be used in SOFC, are [27]:

- Cerium oxide doped with samarium (SDC), $(Ce_{0.85}Sm_{0.15})O_{1.925}$
- Cerium oxide doped with gadolinium (GDC), $(Ce_{0.90}Gd0_{0.10})O_{1.95}$

- Cerium oxide doped with yttrium oped Ceria (YDC), $(Ce_{0.85}Y_{0.15})\,O_{1.95}$
- Cerium doped with calcium (CDC), $(Ce_{0.88}Ca_{0.12})\,O_{1.88}$
- Lanthanum gallate ceramic that include lanthanum strontium gallium magnesium (LSGM), $(La_{0.80}Sr_{0.20})\,(Ga_{0.90}Mg_{0.10})\,O_{2.85}$ or $(La_{0.80}Sr_{0.20})\,(Ga_{0.80}Mg_{0.20})\,O_{2.80}$
- Bismuth yttrium oxide (BYO), $(Bi_{0.75}Y_{0.25})_2O_3$
- Barium Cerate (BCN), $(Bi_{0.75}Y_{0.25})_2O_3$ and
- Strontium Cerate (SYC), $Sr(Ce_{0.95}Yb_{0.05})\,O_3$

For example, changes in ionic conductivity with temperature for various electrolyte materials we can see in Fig.1.4.4.
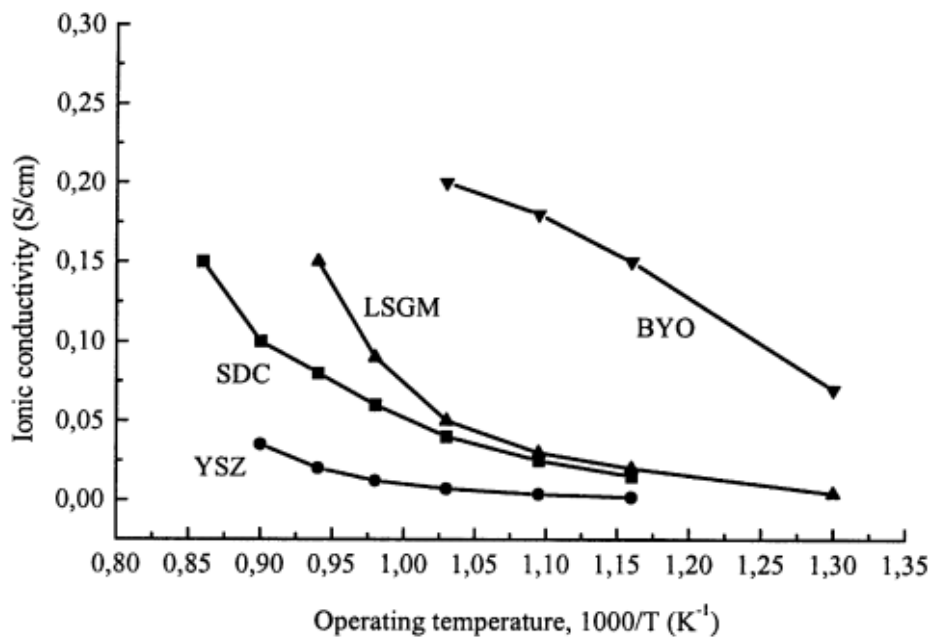
Fig. 1.4.4. Typical ionic conductivity of certain electrolyte materials depending on the operating temperature [28]

1.5. RAMAN STUDY OF CeO₂

The hypothesis of the dependence of oxygen non-stoichiometry on the particle size of nanocrystalline cerium oxide is confirmed by the analysis of Raman spectroscopy data [15]. With the decrease in the size of the CeO₂ particles, systematic changes in the Raman spectra are observed, in particular, a change in the position and width of the peak corresponding to the triply degenerate active mode of F2g (465 cm⁻¹) [15, 16]. The experimental dependence of the half-width of this line on the reciprocal particle size is shown in Fig. 1.5.1 [15,16].
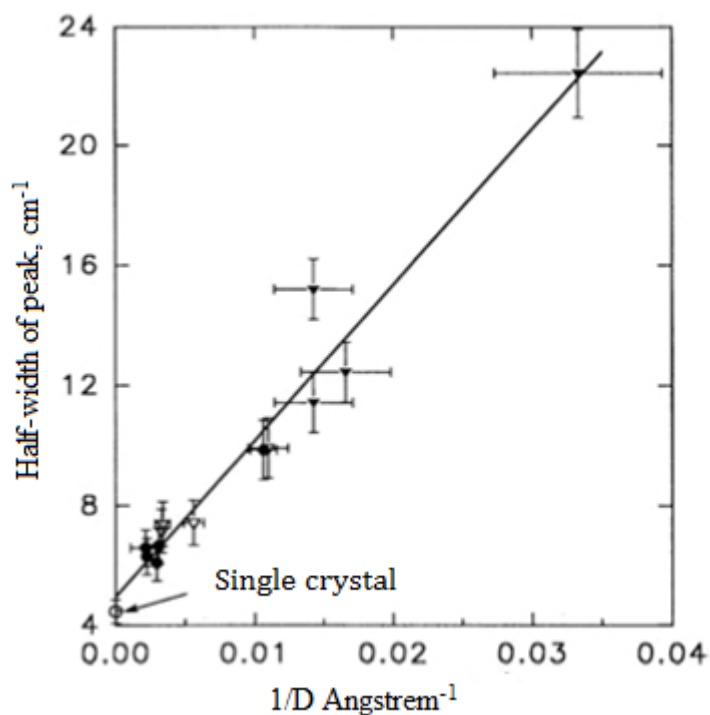
Fig. 1.5.1. Dependence of the half-width of the Raman peak at 465 cm^{-1} on the reciprocal particle size [20]

The Raman mode at 465 cm^{-1}, corresponding to symmetric Ce-O8 vibrations, must be extremely sensitive to any disturbances in the symmetry of oxygen sublattice, including changes in the oxygen stoichiometry of cerium dioxide caused by thermal treatment and / or dimensional effects. This conclusion is confirmed by analyzing the Raman spectra of cerium oxide samples doped with rare earth elements: the observed shifts in the position of the lines mainly depend on the concentration of oxygen vacancies, which is determined by the content of the dopant [15].

Analysis of the Raman spectra of thin-film cerium oxide samples with different particle sizes (4-300 nm) showed that the main effects accompanying the decrease in crystallite size are broadening of the peak at 465 cm^{-1} and simultaneous increase in its asymmetry (Fig. 1.5.2), caused by a decrease in the phonon lifetime typical of nanocrystalline materials [16, 17, 18]. It was once more demonstrated that the half-width of the peak linearly depends on the reciprocal particle size (Fig. 1.5.3); It should be noted that similar dependencies were obtained earlier for other nanocrystalline materials, including Si, Ge, GaAs, etc.
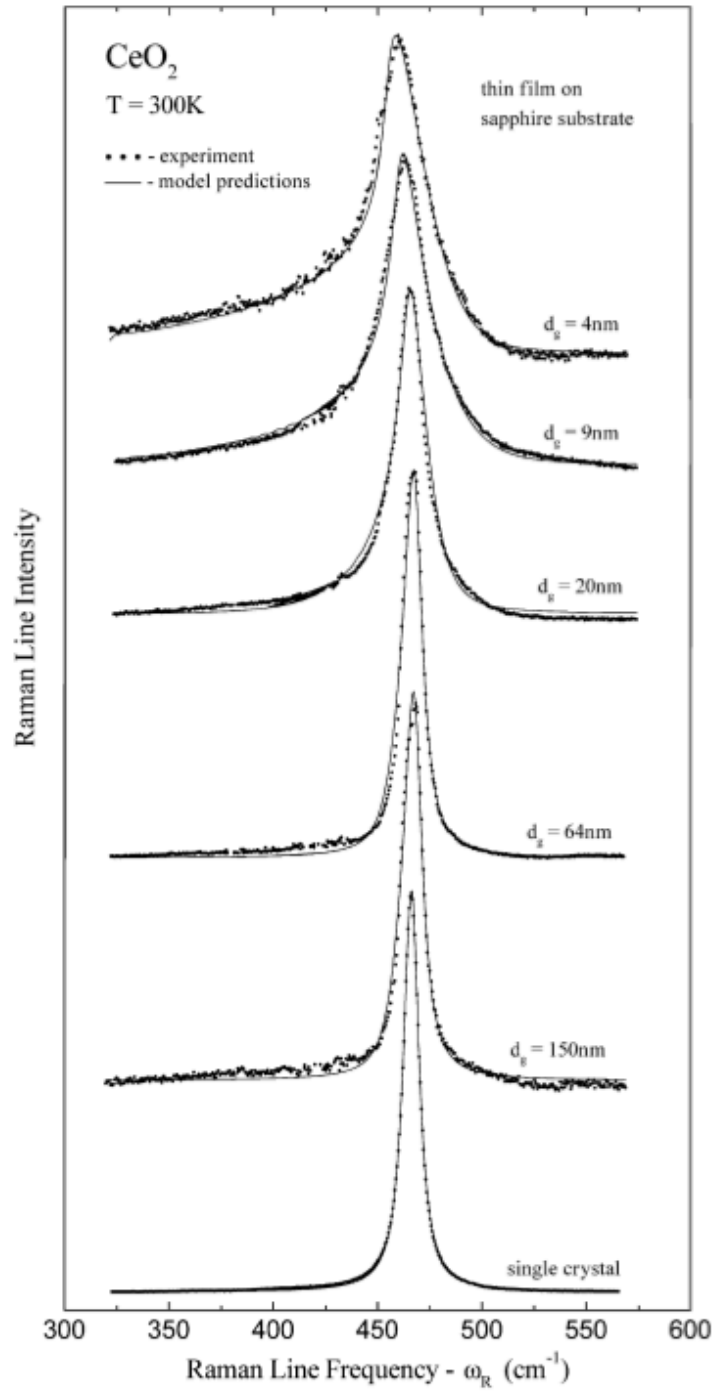
Fig. 1.5.2. Raman spectra of single-crystal and nanocrystalline samples of CeO$_2$ [18]
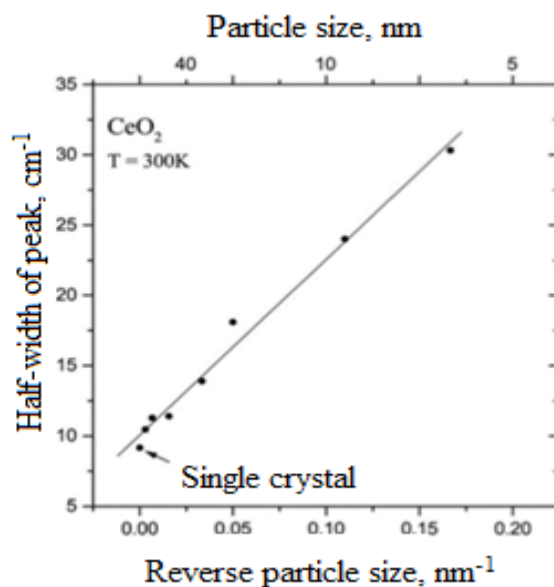
Fig. 1.5.3. The half-width of the peak versus the inverse particle size of cerium oxide [17]

The shift of the Raman peak to the region of lower energies (Fig. 1.5.4) is caused by the increase in the parameter of the crystal cell of cerium oxide with decreasing particle sizes [19]. In turn, the increase in the width of the peak is determined by the presence of inhomogeneous lattice tensions. It is shown that annealing of CeO_2 nanoparticles at high temperatures leads to irreversible changes in the position of the Raman peak (Fig. 1.5.5), which is caused by stress relaxation and / or oxidation of nonstoichiometric cerium oxide [19].
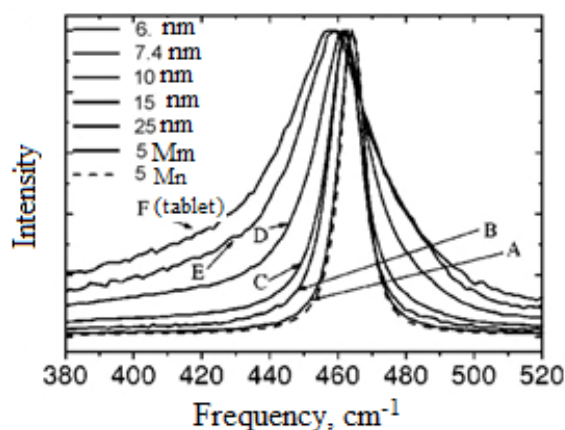
Fig. 1.5.4. Changes in the position, width, and shape of the Raman peak at 465 cm^{-1} with changes in the particle size of the cerium oxide [19]
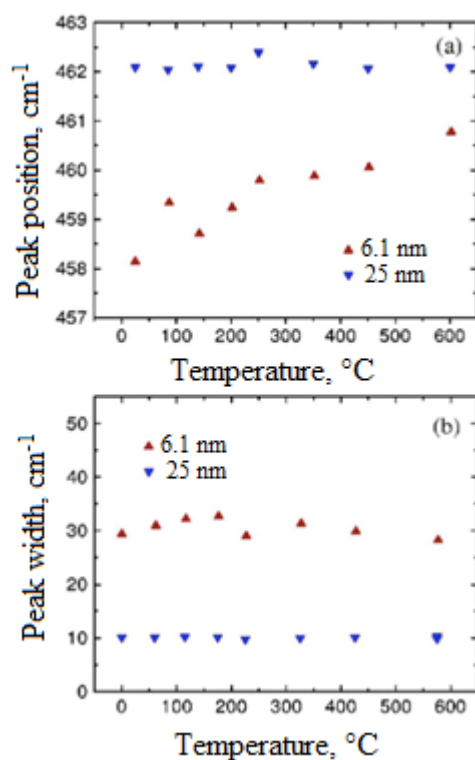
Fig. 1.5.5. Changes in position (a) and width (b) of high-temperature annealing for two nanocrystalline CeO$_2$ samples with different particle sizes [19]

1.6.   APPLICATIONS OF CeO$_2$

The most common rare-earth metal on earth is Cerium [20]. Cerium oxide undoubtedly be called a multifunctional material, based on its wide application in optics, electronics, implementation of gas sensors, humidity, temperature and radiation diesometers, fuel cells (SOFC) etc. The main application area for cerium oxide is the catalytic processes. All these applications are based on its potential redox chemistry between Ce^{3+} and Ce^{4+}, high oxygen affinity and absorption/ excitation energy bands associated with electron structure [20].

According to numerous quantum-mechanical calculations, the energy of formation of oxygen vacancies for cerium oxide decreases with decreasing particle size of CeO$_2$. Moreover, on the scale of particle sizes between CeO$_X$ and macrocrystalline CeO$_2$ clusters (CeO$_2$) there is an area where the energy of formation of vacancies is minimal.
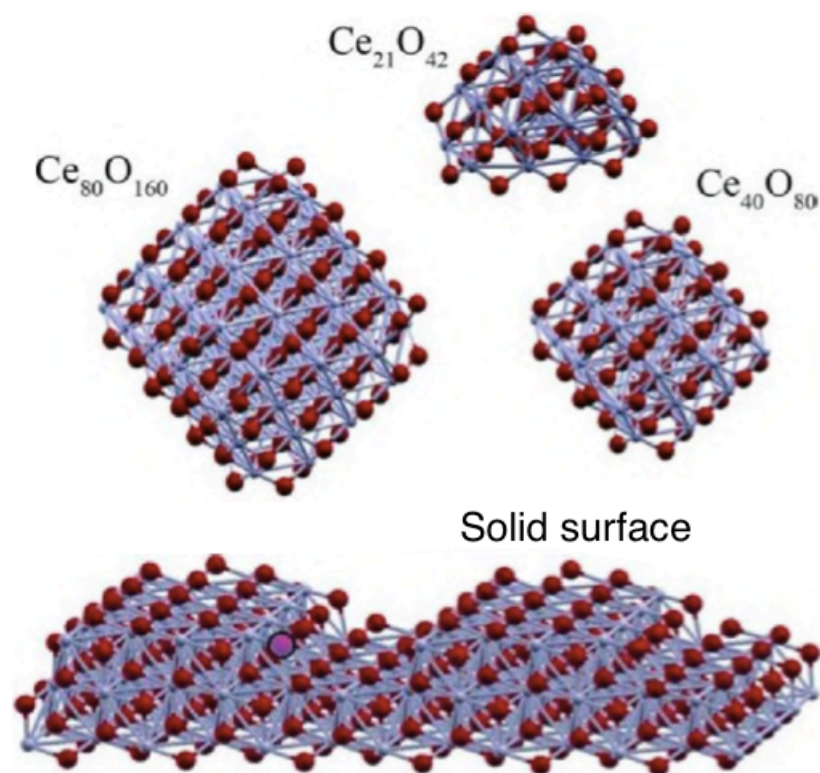
Fig. 1.6.1. Calculation models and the dependence of formation energy of oxygen vacancy on the particle size of CeO_2 [5]

The low energy of formation of oxygen vacancies explains why cerium oxide nanoparticles easily enter oxidation-reduction processes involving active oxygen species. Appropriate studies are actively conducted for inorganic systems, including fuel cells [22], catalysts [23, 22] and gas sensors [5].

In the chemical and petroleum industries, cerium oxide is used as a catalyst. In particular, CeO_2 accelerates the important reaction between hydrogen and carbon monoxide. Cerium oxide has long been successfully used, for dehydrogenation of alcohols.

Cerium oxide (IV) is used in ceramics to create photosensitive glasses. It is also used in the walls of self-cleaning furnaces as a catalyst for the decomposition of hydrocarbons during the high-temperature purification process. The nuclear technology is widely used and cerium containing glass - they do not fade under the influence of radiation. CeO_2 is introduced into the glass as a clarifier and sometimes as a light yellow dye [5, 20].

Cerium oxide is the main component of polyrite, the most effective powder for polishing optical and mirror glass. Polyrite is a brown powder composed of rare earth oxides. The content of cerium oxide in polyrite is not less than 45%. Cerium oxide is used as a catalytic converter to

reduce CO emissions in vehicle exhaust fumes [5, 20].

CeO$_2$ doped with gadolinium and samarium is a useful material for solid oxide fuel cells as they have rather high oxygen ion conductivity at intermediate temperatures [20]. It is possible to use CeO$_2$ in order to increase ionic conductivity and to create a better electrolyte, as this method enables us to create oxygen vacancies in the crystal without adding electron charge carriers. A large number of oxygen vacancies in the electrolyte is formed on the anode (reducing) side of the fuel cell. Some ceric oxides are reduced to cerium oxide under these conditions; this transformation increases electronic conductivity of the material.

Solid oxide fuel cell (SOFC) is one of the most promising ways of generation of electricity from hydrogen and oxygen. SOFC is something like a "factory" in which the input product is fuel and the output product is electricity. And like a factory, the fuel cell operates continuously and produces a product (electricity) only when there is a raw material (fuel) at the input. This is the key difference between batteries and fuel cells. Although both devices work using chemical processes, unlike batteries, fuel cells are not consumed in the course of work. Fuel cells convert chemical energy contained in fuel into electricity.

There are several main advantages of SOFC

- SOFC has the most highest performance (Stream of energy of fuel, therefore power relation).
- SOFC can use different types of fuel: gaseous hydrogen, propane, alcohol and so on.
- SOFC can be produced in very small sizes; this concerns installations for residential, commercial, industrial buildings and even for vehicles.
- SOFC during a release of the significant amount of heat and can be used in the combined cycle (in combination with the gas turbine or a steam boiler).
- Many studies show that SOFCs potentially long-lived: 40000-80000 h.

Solid oxide fuel cells use oxygen-conducting ceramic is an electrolyte. This makes it possible to use as the reducing agent a rather broad class of fuels: from coal and hydrogen to complex alcohols and hydrocarbons [38-41].

Working temperatures, durability and power density of fuel elements are determined by physical-chemical, thermal and other mechanical properties of the materials used and fuel cell components such as electrodes, electrolytes, various electrical connectors, headers, etc [42].

The lattice constant of CeO$_2$ increases under reduced conditions, and the size of nanocrystals decreases as a result of reduction of the cerium cation from Ce (IV) to Ce (III). This increase compensates for the formation of oxygen vacancies, which leads to an increase in the

28

efficiency of the fuel cell.

CeO$_2$ nanoparticles have a particularly high capacity to store oxygen, which is an excellent catalyst due to the ease of transition between trivalent and tetravalent states and high content in nature. CeO$_2$ nanoparticles are most often used in car catalytic converters because of their non-stoichiometric ability to reject oxygen without decomposition. Cerium can release or absorbe oxygen in the exhaust steam of an internal combustion engine, depending on partial oxygen pressure. Due to this mechanism, NOx emissions are reduced, and carbon monoxide is converted into carbon dioxide. Cerium oxide is relatively inexpensive, but its addition significantly reduces the amount of platinum catalyst required for complete oxidation of NOx and other harmful combustion products [26]. Fuel burns more purely when CeO$_2$ is added, which leads to lower air pollution. It has also been described as a useful catalyst in such systems as oxidation of volatile organic carbon and toluene, ozonation of organic compounds and the water-gas shift reactions [20].

1.7. METHODS OF OBTAINING THIN FILMS BASED ON CERIUM OXIDE (CeO$_2$) AND THEIR CHARACTERISTICS

At present, many methods for the synthesis of CeO$_2$ in a thin-film state have been developed, each of which has its advantages and disadvantages. All methods of synthesis of CeO$_2$ films, depending on the nature of the proceeding processes can be divided into three groups: chemical, physical and combined [29] (Fig. 1.7.1).

The classical chemical method for preparation of oxide films of rare earth elements (REE) is the method of modifying the surface of the substrate by thermal oxidation [32], also called "oxidation of the metallic mirror". This method is based on the reaction of oxidation of a layer of metallic cerium newly deposited on the substrate in a stream of air or dry oxygen upon heating. Single-crystal silicon is used as a substrate [30]. As the authors of [30] note, oxidation of Ce occurs within several minutes at 300-350 °C, but films with reproducible parameters cannot be obtained under such conditions.

In [31] synthesis of thin (15 nm) CeO$_2$ films with uniform thickness and stoichiometric composition at 300 ° C in a diffusion furnace in the O$_2$ atmosphere is described. The authors note that the quality of the CeO$_2$ coating depends on the uniformity of the layer of metallic cerium deposited on the substrate [31].

According to the literature data [30, 31] the main drawback of the considered method is the necessity of preliminary deposition of a cerium layer on the substrates, the uniformity of which predetermines the uniformity of the oxide film [30, 31].
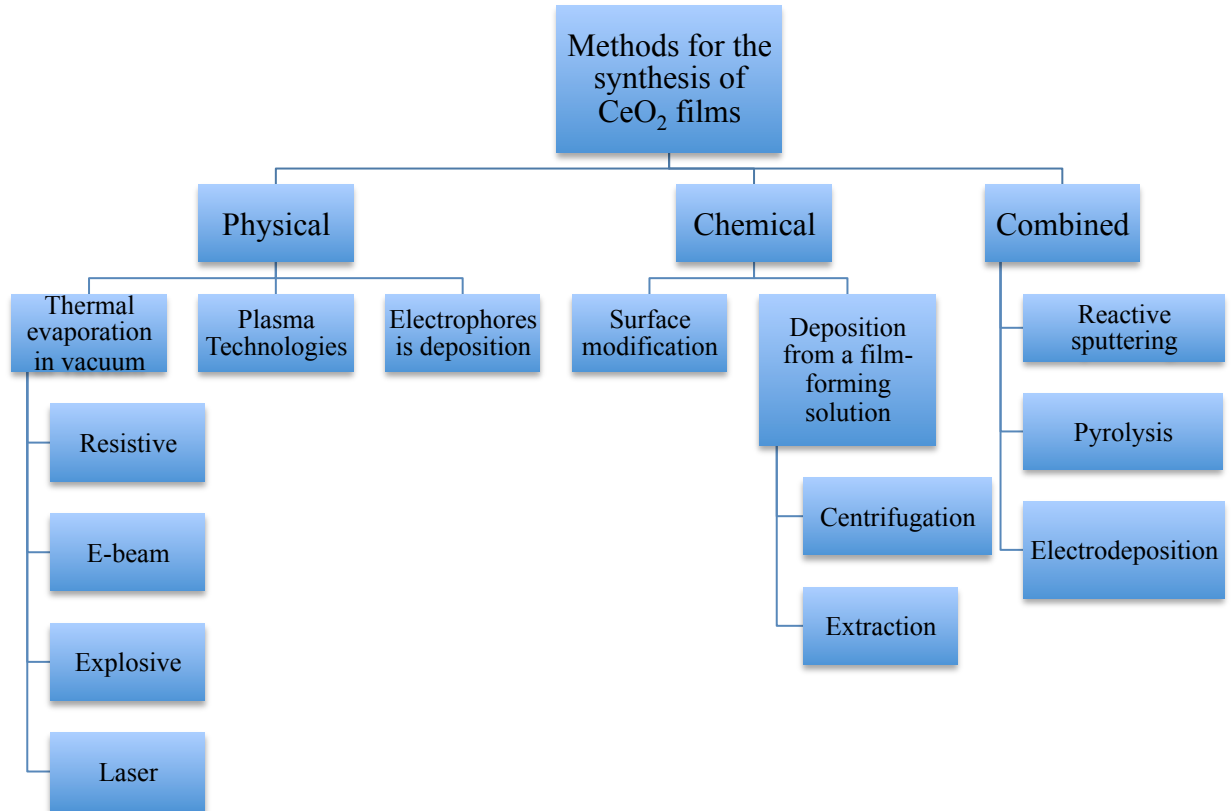
Fig. 1.7.1. - Methods of production of thin films of cerium oxide CeO_2

When choosing film-forming substances, it is necessary to rely on a number of requirements [33]:

- dissolution in various organic polar liquids;

- light hydrolysis in the presence of a small amount of water;

- decomposition during hydrolysis into volatile products of hydrolysis and an insoluble part;

- adhesion of films to the surface of the carrier (possibly due to the presence of functional groups OH–, Cl–, NH_2– and others in the film-forming substance (FFSb)).

These requirements can be fulfilled with the right choice of solvent. Thus, for example, the use of acetone or ethyl alcohol with a small water content (4-6 wt.%) characterized by good wettability of the surface of solid substrates and a low evaporation temperature (T_{ev} = 56.1 and

78.3 ° C, respectively) prevents agglomeration of particles in the film-forming solution, and promotes dissociation and hydrolysis reactions of the film-forming substance [35, 36]. Due to the optimal ratio of the components in the solution, the required viscosity value is reached, the solution acquires a film-forming ability, and firm binding to the substrate forms a homogeneous film in a thin layer. Subsequent heat treatment of the film-forming solution on the substrate leads to the formation of rare-earth oxides, as a result of the decomposition of the intermediate products of hydrolysis of film-forming substances and removal of organic residues.

To depose film-forming solution on the substrate the following methods are used: a centrifugation method, when a certain amount of film-forming solution is deposited on a rapidly rotating substrate with a subsequent redistribution over the entire area under the action of centrifugal forces, and a pulling method based on slow immersion and pulling of the substrate from the solution. Unlike centrifugation, the pulling method allows two-sided coatings to be obtained on substrates of complex shapes. CeO_2 films from film-forming solutions can be obtained on glass [19], nickel [20-23], and other substrates. The method of deposition of films from film-forming solutions has many advantages: it does not require expensive equipment and create a vacuum.

The method of synthesis of CeO_2 films by thermal evaporation in a vacuum consists in heating the evaporated substance (ES) in a vacuum to a certain temperature, and transferring it to a cooler substrate. Depending on the method of heating, this technique is divided into 4 types:

1. **Resistive evaporation**, when the substance is heated by means of a special evaporator heater with ohmic heating.

2. **Explosive evaporation or the "flash" method**, when a small amount of substance is heated instantaneously when it gets on the surface of the evaporator heated by the electric current to the evaporation temperature of the volatile substance.

3. **Electron beam evaporation**, when the local heating of the substance fixed on the anode surface is carried out by bombardment with electron beams emitted by a heated cathode filament [29-36, 38-40, 42].

4. **Laser evaporation**, when the local heating is carried out under the influence of laser radiation [37].

In contrast to the methods discussed above, E-beam and laser evaporation requires preliminary preparation of the substance to prevent electrolysis of individual particles: compression of the CeO_2 powder under pressure followed by calcination in air for 1-5 hours at 1400-1500 ° C or for 6 H at 160 ° C [37]. In the e-beam method, variations in the deposition rate, pressure and temperature of the substrate affect the properties of oxide films. At a deposition rate of 0.01-0.05 nm / s and a pressure of 10^{-6} Torr, polycrystalline CeO_2 films are formed on silicon

substrates [30]. At a rate of 0.05-0.4 nm / s, films with lower crystallinity and high defectiveness of CeO_2 in oxygen are formed [35, 37]. An increase in T_{sub} from 25 to 400 °C leads to an increase in the crystallites of cerium oxide (IV) from 3 to 25 nm, due to their sintering [37].

As the electron source is located in the immediate vicinity of the substance, in the process of electron-beam evaporation, the molecular flow from the substance can be partially ionized and it can react with the cathode material, which leads to a decrease in reproducibility of film properties [9]. The literature review notes that this procedure enables experimenters to increase compactness of obtained films and to decrease the size of CeO_2 crystallites [37].

The method of obtaining films by thermal evaporation in a vacuum is complex from the point of view of the technological process: it is necessary to create a vacuum, to purchase expensive equipment and heaters from a special material, and to maintain the substrate temperature. Despite the need for preparation of the substance (pressing into tablets), the most common methods are laser and e-beam evaporation as they exclude interaction of the substance with the material of the evaporator and, as a consequence, contamination of the films.

Among the plasma technologies for obtaining thin CeO_2 films, high- frequency (HF) (<50 MHz) and radio frequency (RF) (~ 13.56 MHz) magnetron sputtering is used [34]. Magnetron sputtering is the bombardment of the target by high-energy ions from the plasma formed in the working gas by a gas discharge arising when a voltage is applied between the thermionic cathode and anode. The retention of electrons formed in a glow discharge by a magnetic field leads to an increase in the concentration of ions in the plasma, and thereby contributes to an increase in the deposition rate of the films. For spraying, as in the case of laser evaporation, preliminary tableting is necessary.

Many authors state that the temperature of the substrate affects the orientation of films: films with a constant orientation, produced as a buffer sublayer for high-temperature superconductors (HTSC), are formed at Tpolzh. > 870 ° C. The atmosphere and pressure of gases do not affect the oxide composition, on the production of 40-nm thick cerium oxide films by sputtering of the CeO_2 target in an argon flow and a mixture of argon and oxygen. At present, many scientists work at the development of the RF magnetron sputtering method. Sputtering of the CeO_2 target is carried out in the current of O_2, Ar or a mixture of O_2 / Ar at a pressure below 10^{-4} Pa with heating the substrate or annealing films after deposition. This method produces CeO_2 films of different thicknesses: 200 nm (P = 10^{-4} Pa, in a current of O_2 / Ar; T_{sub} = 600 °C) and 0.3-10 nm (P = 10 Pa, in a current of O_2 / Ar; T = 735 ° C). Films obtained by magnetron sputtering have better adhesion than films obtained by the method of thermal evaporation in vacuum at equal sputtering rates, which is explained by higher energy of particles condensed on the substrate, due to which they do not precipitate, but penetrate into the substrate structure [37].

Thus, magnetron sputtering allows us to organize a high-speed production of CeO_2 films of stoichiometric composition with controlled thickness and high adhesion to the substrate. However, this method has some disadvantages – expensive equipment and high energy costs.

Thus, according to the analysis of the literature data, production of thin cerium oxide films can take from several minutes to several days. Regardless of the method chosen, higher deposition time leads to films with larger thickness. Each of the considered methods of synthesis has both advantages and disadvantages.

2. EXPERIMENTAL EQUIPMENT AND METHODS

In this work, the ceramic powder is compressed into a tablet before evaporation. In particular we used (GDC10-T, GDC10-TC GDC20-TC, SDC20-TC, SDC15-TC) with different BET, powder was compressed using a press and deposition rate ranged from 0.2 nm/s to 1.6 nm/s. Wishing to determine how impurities affect their concentration, we used various impurities (CeO_2 with 10 mol% Gd_2O_3 (GDC10), CeO_2 with 20 mol% Gd_2O_3 (GDC20), CeO_2 with 15 mol% Sm_2O_3 (SDC15), CeO_2 with 20 mol% Sm_2O_3 (SDC20)).

2.1. INITIAL SAMPLE SUBSTANCE

Thin films were deposited on different substrates: optical quartz SiO_2, Alloy 600, Si (111), Si (100) and Al_2O_3 by EB-PVD. The main application of ceramic powders and their characteristics are shown in Table 2.1.1.

Table 2.1.1. Characteristics of ceramic powders.

№	Substance	Formula	BET, m^2/g
1	GDC10-TC	$Gd_{0,10}Ce_{0,90}O_{1,95}$	36.2
2	GDC20-TC	$Gd_{0,20}Ce_{0,80}O_{1,9}$	32.8
3	SDC15-TC	$Sm_{0,15}Ce_{0,85}O_{1.925}$	39.3
4	SDC20-TC	$Sm_{0,20}Ce_{0,80}O_{1.9}$	6.2

2.2. ELECTRON BEAM EVAPORATION

Thin films can be formed by various chemical or physical deposition techniques. Electron-beam evaporators depositing thin films of metals, alloys and dielectrics are widely used in industry. Good focusing of the electron beam enables manufacturers to get high concentration of power (up to $5 \cdot 10^8$ W/cm^2) and high temperature giving high rate of evaporation even for the most refractory materials. The rapid movement of the heated zone as a result of deviation of the electron flux, adjustment and control of the heating power and the deposition rate create the preconditions for automatic control of the process. The method effectively uses auto-crucible evaporation of the material providing high purity and uniformity of deposition.

The principle of operation of electron-beam evaporator.

To form the electron beam the electron gun (Fig. 2.2.1), consisting of a hot tungsten cathode and a focusing system is used. The emitted electrons pass through this system, accelerate due to the potential difference of 10 kV between the cathode and the anode, and form an electron beam. The deflection system generates a magnetic field perpendicular to the direction of the electrons coming out of the gun focusing system [43,44].

This field directs the electron beam to the central part of the water-cooled crucible, in the place of beam incidence a local area of heating and vaporization of the liquid phase is formed. The flow of the vaporized material is deposited as a thin film on the substrate, which is usually located at a certain distance above the evaporator. By varying the current in the coil of the electromagnet controlling the deflection system, the operator can scan the beam along the crucible, which prevents the formation of a "crater" in the evaporated material.

In the electron gun free electrons are emitted from the cathode surface, and under the influence of accelerating and focusing electrostatic and magnetic fields the electron beam is formed in the beam, which passes to the working chamber through the outlet. To direct the electron beam to the crucible with the evaporating material and to provide its required parameters, magnetic focusing lenses and deflection systems are used. The free passage of the beam to the object is possible only in a high vacuum. Due to bombardment of the surface by the electron beam, the material is heated to a temperature at which it is evaporated at a requited rate. In the resulting flow the substrate is placed on which volatile substances are condensed. The evaporating unit has measurement and control devices, which are particularly important for control of the electron beam during the deposition process [43-45].

In the simplest case, the electron beam is directed onto the evaporated material vertically from the above or at an oblique angle to the surface. To focus the beam on the surface and to obtain the required power density on the material the long-focused generators of electron beams are used. Significant disadvantages of this arrangement is the possibility of formation of a film on the details of the electron-optical system, which may change parameters of the electron beam, and limitation of the useful area for placement of the substrate because of the shading of the part of the chamber by the gun. These disadvantages can be avoided by placing the gun horizontally and deflecting the electron beam on the evaporating material using the systems providing rotation of the beam at an angle of up to 270 °.
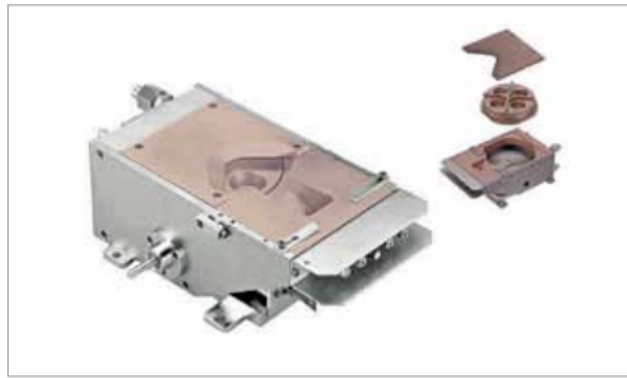
Fig. 2.2.1. An electron gun [23]

As a rule, the electron beam evaporator (Fig. 2.2.2, 2.2.3) consists of three main parts: an electron gun, a deflection system and a water-cooled crucible vessel of variable capacity (7, 13, 15, 18, 25, 40 and 156 cm^3). This provides continuous operation without addition of evaporating material, which does not contact in the molten state with the copper walls of the crucible. In general, it is possible to use a material molded by the size of the crucible (evaporation without crucible) or powder in combination with special crucibles [43-45].
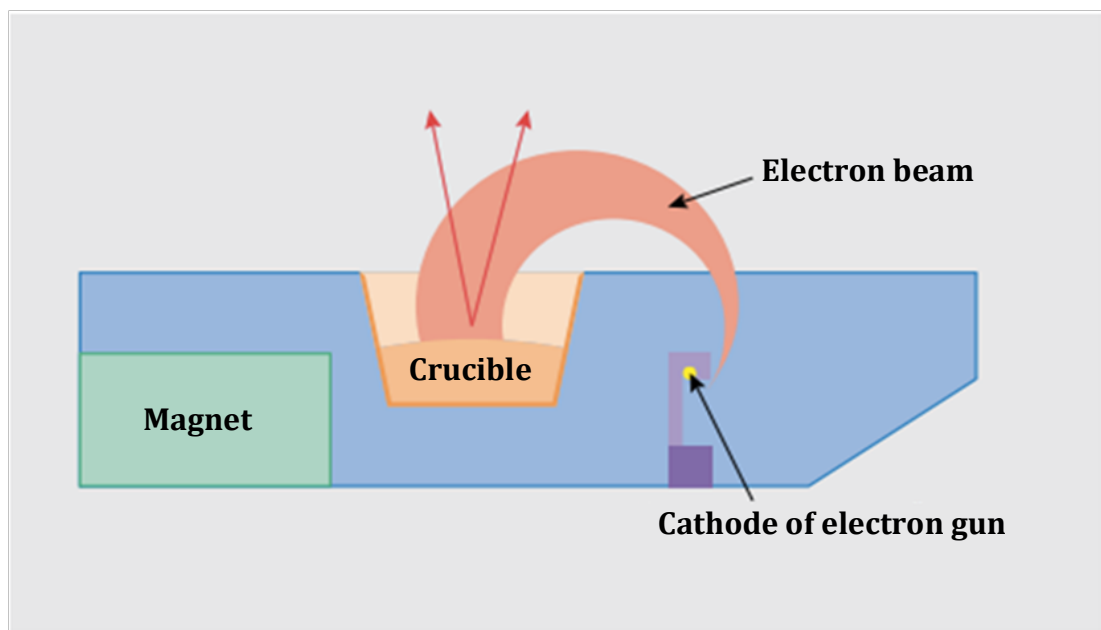
Fig. 2.2.2. A scheme of an electron-beam evaporator [23]

The electron beam evaporator is located in a chamber with a vacuum level of 10^{-4} Pa, required to minimize the influence of the residual gas on the passage of the electron beam and to exclude the contamination with other materials of the resulting film.
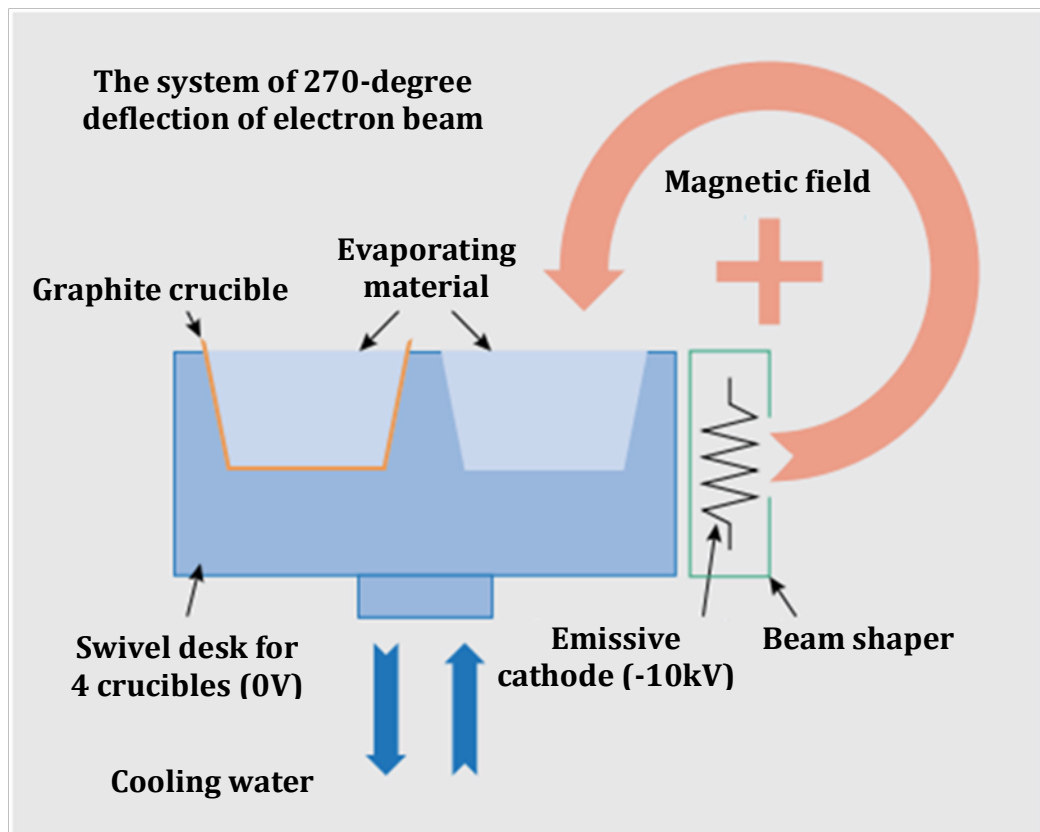
Fig. 2.2.3. A scheme of creation of the electron beam and the rotary working table [23]

About 30-40% of the power of the electron beam goes on melting and evaporation of the material (2-10% and 30-35%, respectively). The other part of the power is spent on heat transfer by conduction and radiation and is removed by electrons emitted from the heated zone. This power depends on the nature of the evaporated material and parameters of the electron beam. The main portion of energy is removed by inelastically reflected electrons, the number of which is determined primarily by the nature of the material (for steel - about 25% of the power, for tungsten - 38%)[43-45].

Advantages of the electron-beam evaporation:

• Possibility of applying metal films (including refractory), alloys, semiconductors and dielectric compounds with melting points up to 3,500 ° C;

• High rate of evaporation of substances (1 to 10 nm / m) and possibility of its control in a wide range by varying the power supplied to the evaporator;

• Possibility of obtaining coatings with high vacuum, practically free from impurities; their purity is determined by the purity of the material used for spraying;

• Uniformity of produced coatings;

• Free diffusion of atoms of the material of the evaporator in the chamber, their rectilinear movement without colliding with residual molecules of the air components and useless

dispersion of the material in the chamber volume, no chemical interaction of the sputtered material with air residues [44,45].

The equipment on which we worked was produced by Kurt J. Lesker Company® PRO Line PVD 75. Along with the magnetron sputtering equipment, it provides equipment for film formation by electron-beam method, in particular, E-Beam Evaporator. We chose the electron-beam method.

The equipment on which we worked, in particular, E-Beam Evaporator is shown in Fig. 2.2.4. Thin film formation with the use of (PVD 75) and all analysis was made in Lithuania Energy Institute, Center for Hydrogen Energy Technologies.

Fig. 2.2.4. E-Beam Evaporator (PVD 75) [44]

The setup consists of the working chamber, control panel with an electron beam (PC, the sensor controlling the coating thickness) and the cryopump. The following units are placed separately:

• rotary pump (the first stage of the two-stage pumping of the working chamber);

• cryocompressor to maintain the temperature of the cryo pump;

• transformer AC 380/220 V (three phases), from which the installation and its external components are powered [44].

Table 2.2.1 summarizes the characteristics of the installation.

Fig. 2.2.5. The working chamber of the E-Beam Evaporator (PVD 75)

Fig. 2.2.5 shows the working chamber of the installation. It includes an evaporator consisting of an electron beam gun with a beam deflection system deflecting the beam up to 270°. In addition, the chamber is equipped with a crystal oscillator, which controls the deposition rate in the real time and the final coating thickness with angstrom accuracy.

Table 2.2.1. Technical characteristics of E-Beam Evaporator.

Electron beam source	Current tungsten filament	50A (when 10 kV)
	Accelerating voltage	4–10 kV ±0.5%
	Beam power	Up to 6 kW, voltage 10 kV
	Beam deflection	270°
	Beam shape	Sine, sawtooth, triangle, arbitrary
	The maximum electron	600mA
Crucible		15 sm^3 , 4 units (depending on the size)
System of automatic measurement of beam thickness	Sensor type	Quartz oscillator, the frequency of 6 MHz
	Resolution	±0.028 Hz
	Measurement interval	0.25 s
	Resolution of film	0.034 Å
Maximal vacuum		$5×10^{-7}$ Torr
Unit for substrate heating		Two pairs of IR lamp heaters with a maximum temperature of 450 ° C
Heating block substrates		Heater with a maximum temperature of 600 ° C
The diameter of the focused beam		3mm
The maximum speed of evaporation in a		12000 Å/min
working pressure		10^{-1}Pa , 10^{-6}-Pa

2.3. EXPERIMENTAL PARAMETERS IN THE FORMATION OF THIN FILMS

Thin films can be formed by various chemical or physical deposition techniques. As mentioned previously, e-beam was chosen because electron beam evaporation enables us to form a film of desired thickness and homogenuity. Electron-beam evaporation is a process during which the evaporating substance shelled electrons. The kinetic energy of these electrons is transformed into thermal energy and heats the evaporating substance. The substance evaporates and is deposited on the substrate surface. Thus, a new surface (thin films) is formed on the substrates [26].

The initial pressure of the chamber was 2.5×10^{-6} then the pressure was changed because there was burning oxygen in the chamber. During the experiment, the voltage was constant 7.9 kV. Wishing to evaporate the substance sprayed on the entire area of the film substrate we rotated at 8 rpm.

Sm doped cerium oxide thin films (~1.9 μm) were deposited on SiO_2, Alloy 600 (Fe-Ni-Cr), Si(111), Si (100) and Al_2O_3 substrates. Such substrates were chosen for the reason that SiO_2 substrate is amorphous and it does not affect the microstructure or the morphology of thin films. Al_2O_3 was chosen due to its high melting temperature (2345 K) and low electrical conductivity. Alloy600 (Fe-Ni-Cr) could be used as interconnector in IT-SOFC, and Ni-SDC is considered to be a good choice for anode in IT-SOFC. The substrates were ultrasonically cleaned in pure acetone for 10 min. Thin films were formed with e-beam physical vapour deposition system "Kurt J. Lesker EB-PVD 75", using deposition rate 0.2 nm/s ÷ 1.6 nm/s and also we changed substrate temperatures from 50 ^{o}C K to 600 ^{o}C step-by-step. The working pressure for all samples was $5 \cdot 10^{-7}$ bar. The $Sm_{0.2}Ce_{0.8}O_{2-\delta}$ powder (Nexceris, LLC, Fuelcellmaterials, USA) of 6.2 m^2/g surface area was used as evaporating material. It was pressed into the pellets using mechanical press (303.5 MPa pressure). The pellets were placed into crucible and vacuum chamber was depressurised up to $2 \cdot 10^{-9}$ bar. After that, the substrates were treated with Ar+ ion plasma (10 min) and preheated up to working temperature. Thickness and deposition rate were controlled with INFICON crystal sensor.

2.4. METHODS OF INVESTIGATION OF FORMED CERAMIC THIN FILMS

Diffraction of X-rays (XRD, X-ray). This diffraction method is used to study the structure of thin films (the size of the crystals, the lattice parameters) and to calculate the texture coefficient. The measurements were performed with X-ray diffractometer D8 Discover (Bruker AXS GmbH). The results were processed using the computer program DIFFRACplus EVA. The basic parameters of the X-ray diffractometer are presented in Table 2.4.1.

Table 2.4.1. Technical parameters of X-ray diffractometer.

Configurations	Horizontal or vertical goniometer, Theta/2Theta or Theta/Theta geometry
Angular range (without accessories)	360°
Max. usable angular range (depending on accessories)	$-110° < 2Theta \leq 168°$
Maximum angular speed (depending on accessories)	20°/s
Smallest addressable increment	0.0001°

Scanning electron microscope (SEM). Scanning electron microscope(SEM Hitachi, S-3400N) is used to analyze the surface structure and morphology. The magnification is from 5 up to 300 000. Accelerating voltage is from 0.3 to 30 kV. Scanning electron microscope has the prefix for the X-ray microanalysis, which is designed to determine the chemical composition of solid samples. The detection limit is about 10-2 wt. %, the minimal field of study is 1 micron for elements. X-ray fluorescence analysis for elemental composition. The detection limit is about 10–5 wt. %, the minimal field of study is 100 microns. The resolving power when using the secondary electron detector – 3.0 nm (accelerating voltage 30 kV, when working with a high degree of dilution); 10 nm (3 kV accelerating voltage, when working with a high degree of dilution). The resolution of the detector when using backscattered electrons - 4.0 nm (accelerating voltage 30 kV, when working with a low degree of dilution).

Electron dispersive spectroscopy (EDS). The energy dispersive spectrometry (EDS, Bruker AXS Microanalysis GmbH) has been used for determination of the elemental composition of thin films, based on the analysis of X-ray emission energy spectrum. In our case EDS Equipment is connected to the SEM. With the help of electron beam or X-ray sample atoms are excited, emitting a characteristic for each chemical element X-ray radiation. Investigating the energy spectrum of the radiation, it is possible to draw conclusions about the qualitative and quantitative composition of the sample. We used EDS spectrometer (Bruker XFlash)

Raman spectroscopy. The Raman effect arises when a photon is incident on a molecule and interacts with the electric dipole of the molecule. In quantum mechanics the scattering is described as an excitation to a virtual state lower in energy than a real electron transition with nearly coincident deexcitation and a change in vibrational energy [5]. To register the Raman spectra, installations with different beam geometries and different polarizers on the incoming or outgoing beams are used. The geometry of the system (the angle between the incident and registered beams) determines which components of the induced dipole moment contribute to the line intensity.

The Raman spectroscopy (Confocal Raman spectrometer Solver Spectrum (NT-MDT, Russia)) is equipped with three lasers (633, 532, 473 nm) There are three diffraction gratings providing different spectral resolution (1800/500, 600/600, 150/500). CCD camera detector iDus (Andor) is cooled down to -65 $^{\circ}$C. From the analysis of the Raman spectra it is possible to obtain information about the oxygen vacancies in the structure of fluorite, whose number and energy of the cation, dopant-vacancy determine the transport properties of the material.

Fig. 2.4.1. General view of Confocal Raman spectrometer Solver Spectrum (NT-MDT, Russia)

When making measurements, the following conditions must be observed:

- ambient air temperature (15 - 30) $^{\circ}$ C;

- atmospheric pressure (700-770) mmHg;

- relative humidity of air (20-80)%;

- voltage in the electrical network (220 ± 10) V.

Light incident on the sample can be reflected, absorbed, or scattered. The process of light scattering is elastic (i.e., there is no energy exchange between light and matter) and inelastic (i.e., there may be a redistribution of energy between light and matter).

Elastic light scattering is called Rayleigh scattering (RS). It is a predominant process: on average, only one photon out of ten million undergoes inelastic scattering. In Rayleigh scattering, the frequency of scattered light is exactly equal to the frequency of incident light.

Inelastic light scattering is called Raman scattering. In Raman scattering, light and matter exchange energy. As a result, the frequency of the scattered light can decrease (in this case the energy passes from light to matter – this is Stokes scattering), and increase (in this case the energy passes from matter to light – this is anti-Stokes scattering).
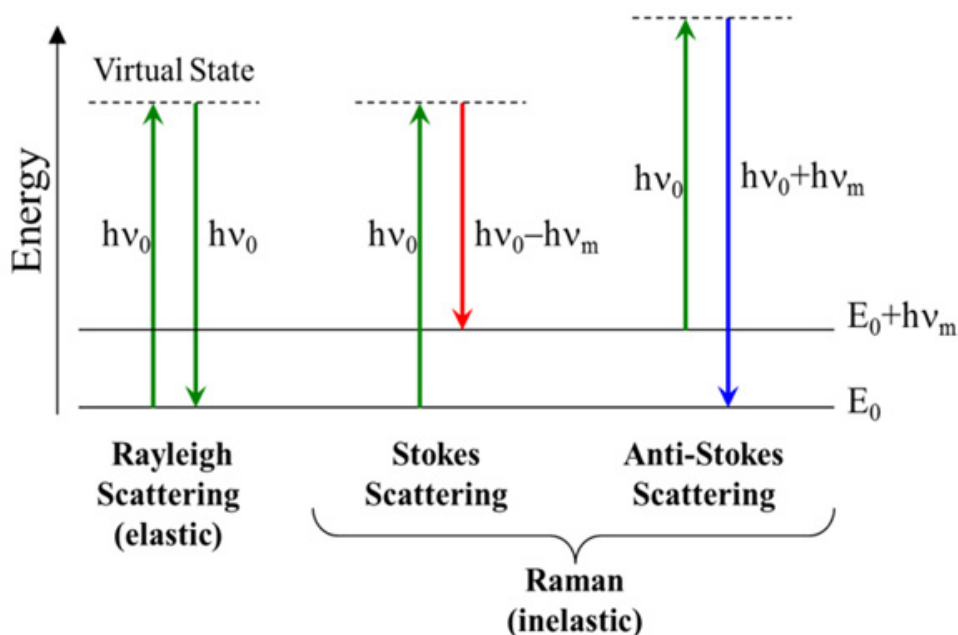
Fig. 2.4.1. Energy-level diagram showing the states involved in Raman spectra

In Rayleigh scattering, the molecule absorbs a photon from the zero vibrational level, and then goes to it after radiation. In Stokes scattering, the molecule absorbs a photon from the zero vibrational level, but after radiation goes to the first level, absorbingh part of the photon energy. Conversely, in case of anti-Stokes scattering, the molecule absorbs a photon from the first vibrational level, and after radiation goes to the zero level, giving part of its energy to the emitted photon. Under the conditions of thermal equilibrium, the population of vibrational levels obeys the Boltzmann distribution, that is, the population of the higher levels decreases exponentially. Hence, the first level is populated much less than the zero level, which gives

43

much lower intensity of the anti-Stokes lines in the Raman spectrum than the intensity of the Stokes lines.

The Raman spectrum of most organic molecules consists of lines corresponding to deformation and valence vibrations of carbon (C) chemical bonds with other elements, usually hydrogen (H), oxygen (O) and nitrogen (N), as well as characteristic vibrations of various functional groups (hydroxyl-OH, amino groups -NH_2, etc.). These lines appear in the range from 600 cm^{-1} (valence vibrations of single C-C bonds) to 3600 cm^{-1} (vibrations of the hydroxyl group). In addition, in the spectra of organic molecules in the range 250-400 cm^{-1}, deformation vibrations of the aliphatic chain appear.

The Raman spectra of crystal lattices contain lines corresponding to the scattering of radiation by collective excited states of the lattice, which in solid state physics are regarded as quasiparticles. The most common are Raman-active transitions involving optical and acoustic phonons, plasmons, and magnons.
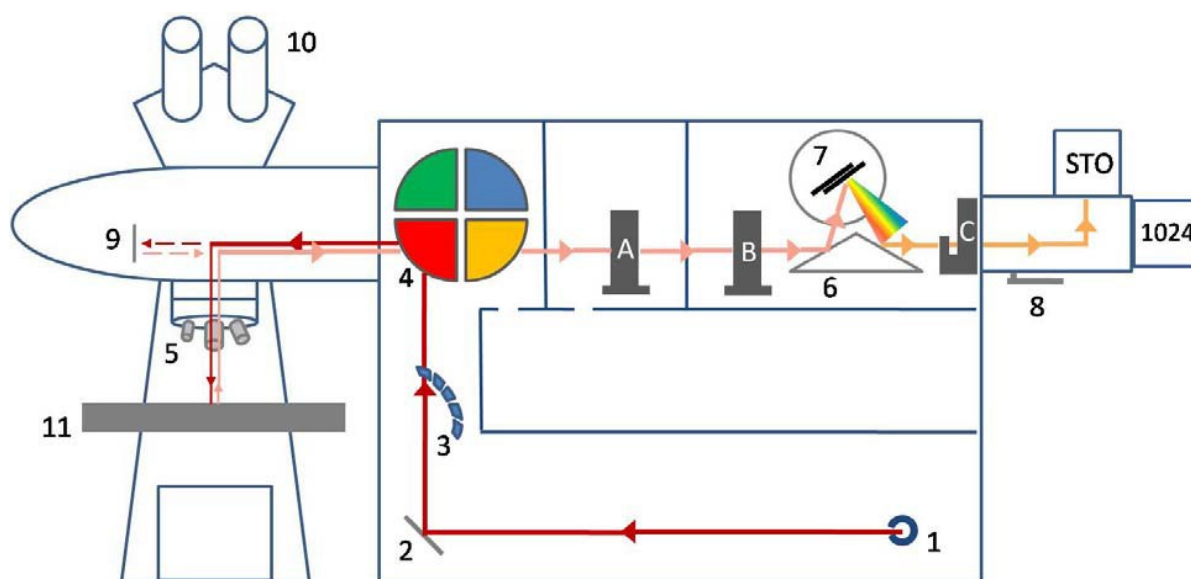
Fig. 2.4.2. Scheme of Solver Spectrum (NT-MDT), Russia

The beam of laser radiation enters the device through the inlet 1, reflects from the mirror 2, passes through one of the lenses 3 and hits the light filter 4. For the incident beam, the light filter acts as a mirror and directs it through the optical system 5, including the microscope objectives, onto the sample. The radiation scattered by the sample comes back to the filter 4, which transmits only inelastically scattered light. The beam passes through the lenses A and B and is reflected from the mirror 6. The diffraction grating 7 decomposes the light into the spectrum, and the desired wavelength is directed through the lens C to one of the detectors. The detectors are switched by the lever 8. Inside the microscope case there is an internal

standard (silicon) used for aligning the device. The sample is observed through the eyelens 10. The microscope table 11 has a system of mechanical and electrical control.

Table 2.4.2. Parameters and mode of shooting Raman spectra for samples(GDC10-T, GDC10-TC, GDC20-TC, SDC15-TC, SDC-TC (0.2nm/s-1.6nm/s)).

Laser wavelength	Grating	Detector	Shooting mode	Sample
532nm Green Laser	1800/500	iDus (Andor)	CCD camera	SDC-TC (0.2nm/s-1.6nm/s)
532 nm Green Laser	1800/500	iDus (Andor)	CCD camera	GDC10-T
532 nm Green Laser	1800/500	iDus (Andor)	CCD camera	GDC10-TC
532 nm Green Laser	1800/500	iDus (Andor)	CCD camera	GDC20-TC
532 nm Green Laser	1800/500	iDus (Andor)	CCD camera	SDC15-TC

3. RESULTS AND DISCUSSION

Thin films can be formed by various chemical or physical deposition techniques. As mentioned previously, we chose as a e-beam because electron beam evaporation permits a desired thickness to form a film, and a film thin and homogeneous. In work, the ceramic powder is compressed into a tablet before evaporation. In particular we use (SDC-TC (0.2nm/s-1.6nm/s), GDC10-T, GDC10-TC, GDC20-TC, SDC15-TC), powder compressed using a press. Wishing to determine how impurities affect their concentration, were used various impurities (CeO_2 with 10 mol% Gd_2O_3 (GDC10), CeO_2 with 20 mol% Gd_2O_3 (GDC20), CeO_2 with 15 mol% Sm_2O_3 (SDC15), CeO_2 with 20 mol% Sm_2O_3 (SDC20)).

To determine the concentration and size of nanocrystallites of thin films, three experimental methods are used: Raman spectroscopy, X-ray diffraction. Comparing these two methods one can say that Raman spectroscopy is one of the most frequently used methods, since Raman spectroscopy is reliable due to locality, expression and non-destructive effects of the object under study.

In the Raman spectrum, the Raman shift expresses the frequency shift between the incident laser light and the scattered light as [34]:

$$\Delta \nu (cm^{-1}) = \nu_L - \nu_R = \frac{10^7}{\lambda_L (nm)} - \frac{10^7}{\lambda_R (nm)} \qquad (4)$$

where ν_R and ν_L represent the absolute wave number of the scattered light and that of the laser respectively. ν_L has a fixed value depending on the laser [34]: in our case $\nu_L = 18796.99$ cm^{-1} 532nm green laser.

3.1. DIFFRACTION OF X-RAYS

Measurement of thin film X-ray diffraction spectra (XRD, X-ray) was carried out through the program (DIFFRACTplus EVA). The crystallite size was calculated using the program (TOPAS). The results of X-ray diffraction analyses are shown in two comparisons of the deposition rate and substrate temperature. By X-ray diffraction, we obtained that all thin films (SDC) based on cerium oxide have a single-phase and fluorite structure with space group Fm3m.
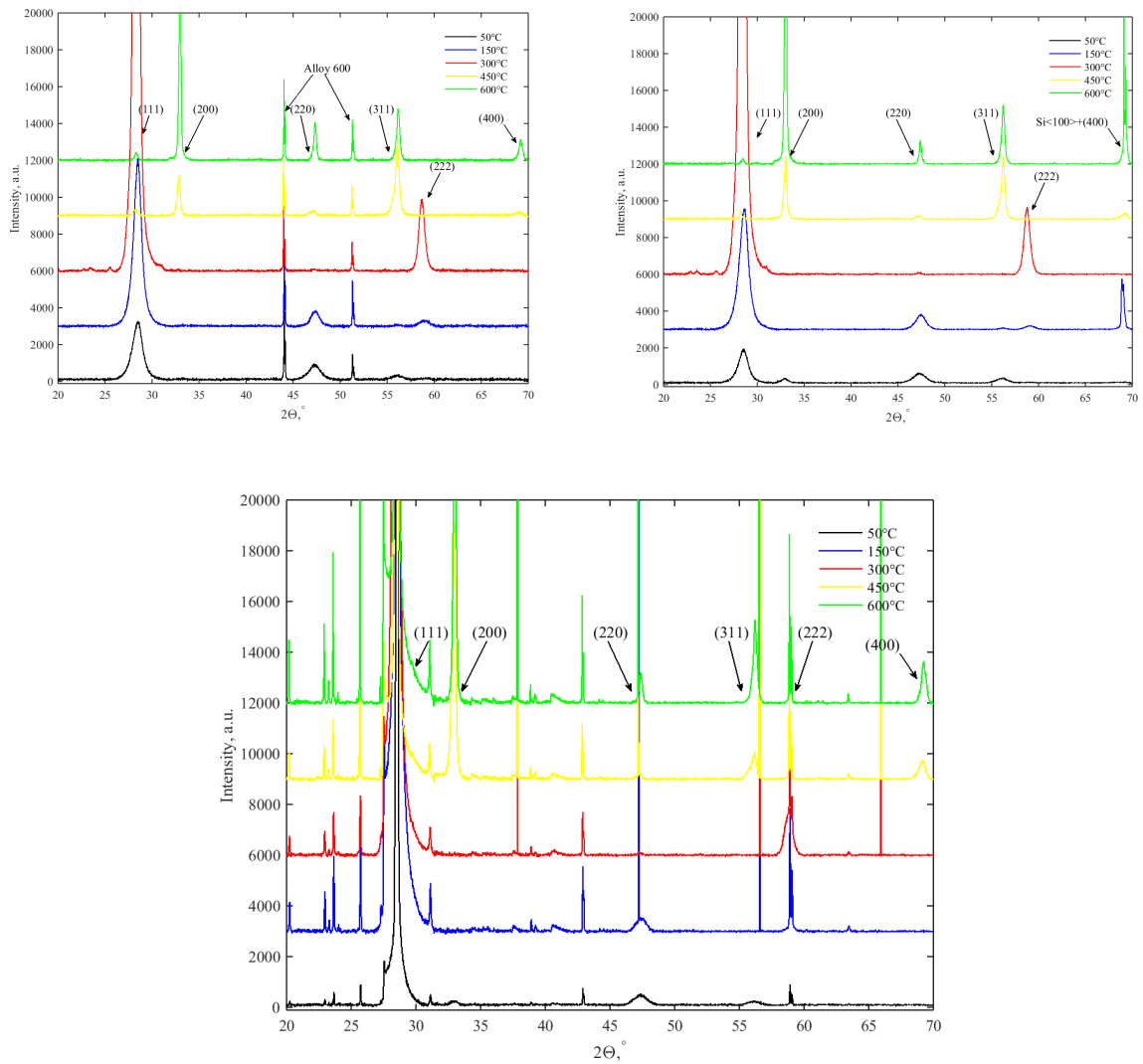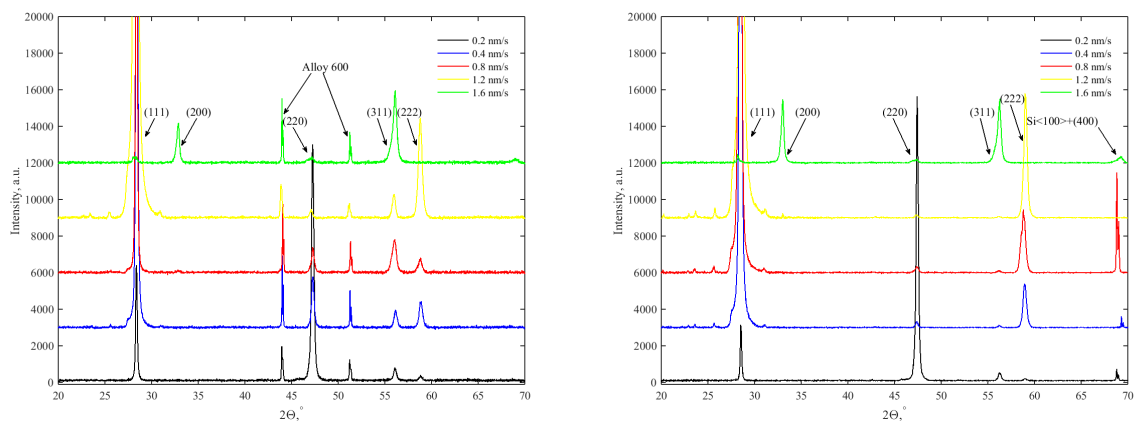
Fig. 3.1.1. XRD patterns of (SDC) deposition rate of 1.6 nm thin ceramic deposited on a) Alloy 600 and b) Si (100), c) Si (111)

X-ray diffraction patterns of SDC thin films have characteristic peaks, corresponding to crystallographic orientations (111), (200), (220), (311), (222), and (400) (Fig. 3.1.1, 3.2.1 Table 3.1.1.).
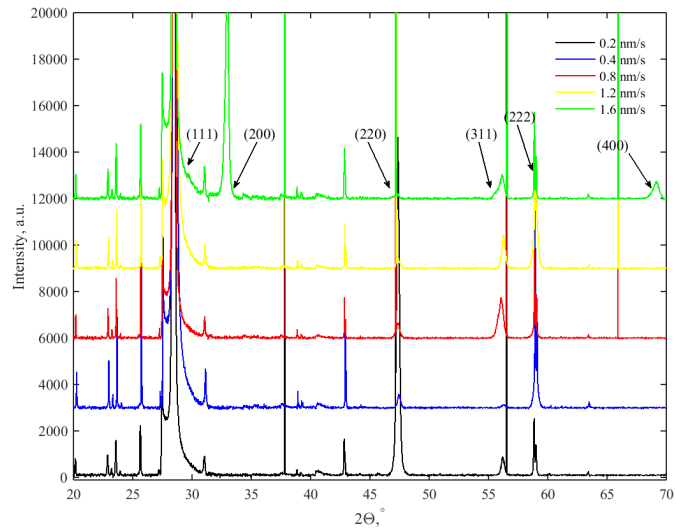
Fig. 3.1.2. XRD patterns of (SDC) deposition rate of 0.2nm - 1.6 nm thin ceramic deposited on a) Alloy 600 and b) Si (100), c) Si (111) at a temperature 450 $^{\circ}$C

As we can see in Fig. 3.1.1 and 3.1.2 for all films with CeO_2 cubic structure mostly dominates at the surface (111). All ceramic thin films do not retain the same structure and orientation, since the deposition parameters were different, as we know from the literature, analysis of thin films of identical components at different deposition parameters can give different structure and orientation.

Table 3.1.1. Thiknes of thin film h, nm and Crystallite size (‹d› SiO_2 and ‹d› Alloy) dependence on deposition rate (v_g) and substrate temperature (T_S) of thin films formed on Alloy 600 and SiO_2 substrates.

			Crystallite size		Lattice constant	
v_g, nm/s	T_{sub}, °C	h(film), nm	$<d_{SiO2}$, nm>	$<d_{Alloy600}$, nm>	a_{SiO2}, nm	$a_{Alloy600}$, nm
0.2	50	2814	9,7	16,3	5,4341	5,4329
0.2	150	1006	16	25,1	5,4289	5,4308
0.2	300	2387	28,7	39,3	5,4264	5,4259
0.2	450	1584	80,6	57	5,4266	5,429
0.2	600	1389	66,2	54,8	5,4298	5,4288
0.4	50	2524	7,9	13,6	5,4338	5,4312

|						
0.4	150	2079	19,9	30,4	5,4299	5,4261
0.4	300	1790	30	50,7	5,4324	5,4299
0.4	450	1661	62,4	55,38	5,4286	5,4284
0.4	600	1857	48,7	67,8	5,4335	5,4358
0.8	50	2441	7,5	11,3	5,4388	5,4335
0.8	150	2061	12,1	19	5,4278	5,4236
0.8	300	2060	21,9	27,3	5,4308	5,4314
0.8	450	1579	46,1	58	5,4292	5,4384
0.8	600	1351	66,5	48,8	5,4318	5,4301
1.2	50	2296	10,2	11	5,4469	5,4354
1.2	150	1943	15,2	19,7	5,4456	5,4469
1.2	300	2671	22,7	31,3	5,4251	5,4249
1.2	450	2048	31,4	43,7	5,426	5,4257
1.2	600	1603	50,2	45,7	5,4218	5,4231
1.6	50	2432	6,8	7,5	5,4455	5,44
1.6	150	2491	6,9	9,6	5,4393	5,4279
1.6	300	2585	17,8	26,8	5,4432	5,4435
1.6	450	1486	25,3	25,8	5,4418	5,4252
1.6	600	1531	48	62,2	5,4273	5,4287
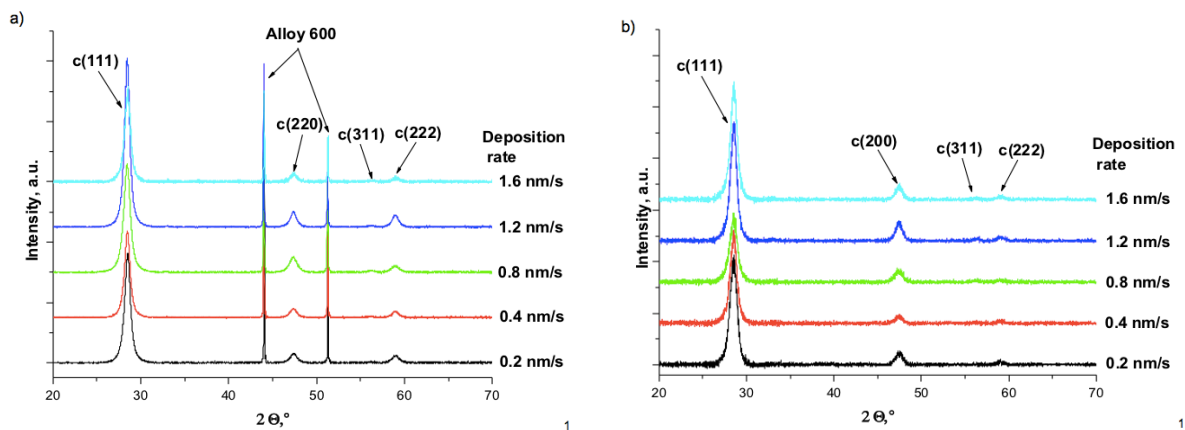
Fig. 3.1.3. XRD patterns of (GDC 10) deposition rate of 0.2nm - 1.6 nm thin ceramic deposited on a) Alloy 600 and b) SiO_2
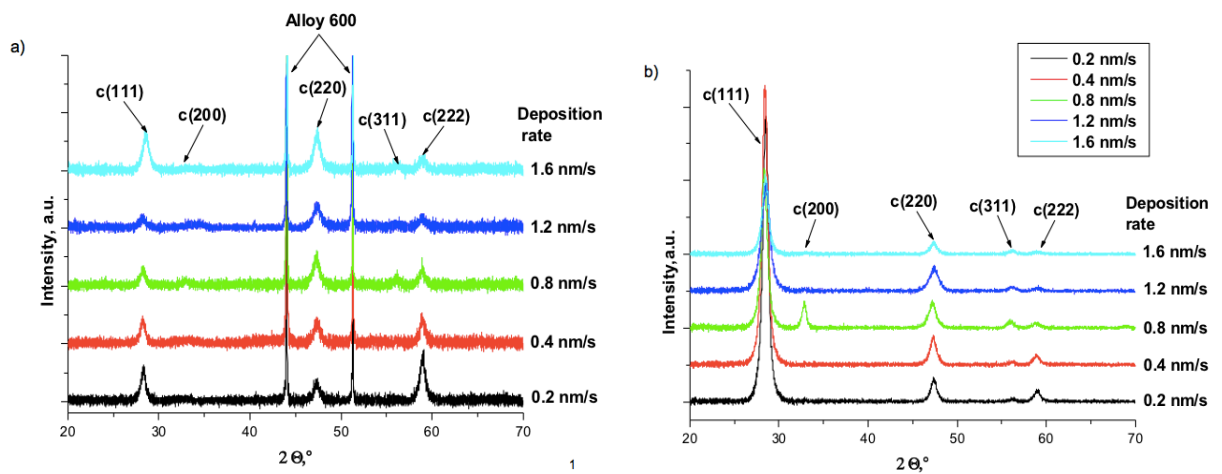
Fig. 3.1.4. XRD patterns of (GDC 20) deposition rate of 0.2nm - 1.6 nm thin ceramic deposited on a) Alloy 600 and b) SiO$_2$
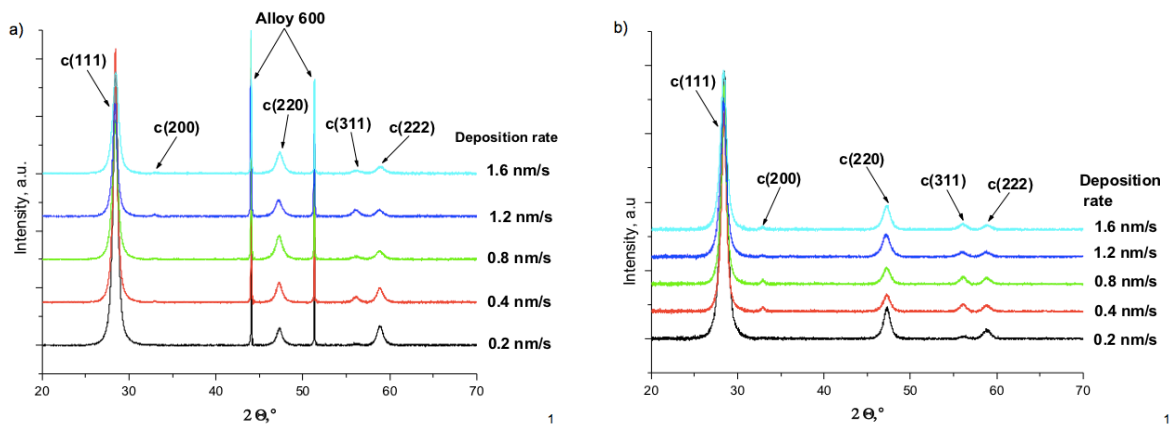
Fig. 3.1.5. XRD patterns of (SDC 15) deposition rate of 0.2nm - 1.6 nm thin ceramic deposited on a) Alloy 600 and b) SiO$_2$

GDC10 and GDC20 thin films X-ray diffraction (Fig. 3.2.3. - 3.2.5.), we can say that all source powders have the same cubic phase, and show the same crystallographic orientation: acute (111) and minor (200), (220), (311) and (222) orientation. In case of GDC20 dominant crystallographic orientation (111) the intensity of the peak decreases. This orientation may be associated with deposition energy of the particles, which can migrate into larger clusters changing the dominant peak intensity. In the analysis of X-ray spectroscopy, the more intense peaks of a narrow line width shown in Fig. 3.1.2 may indicate an increase in the grain size with an admixture of Sm^{3+}.

3.2. INVESTIGATION OF THE SURFACE USING SEM

In order to study the morphology of a thin film we did m pictures. The surface investigations were conducted using scanning electron microscope (SEM Hitachi, S-3400N). SEM pictures are shown in the same magnification x 40k, to compare the morphology of the coating.

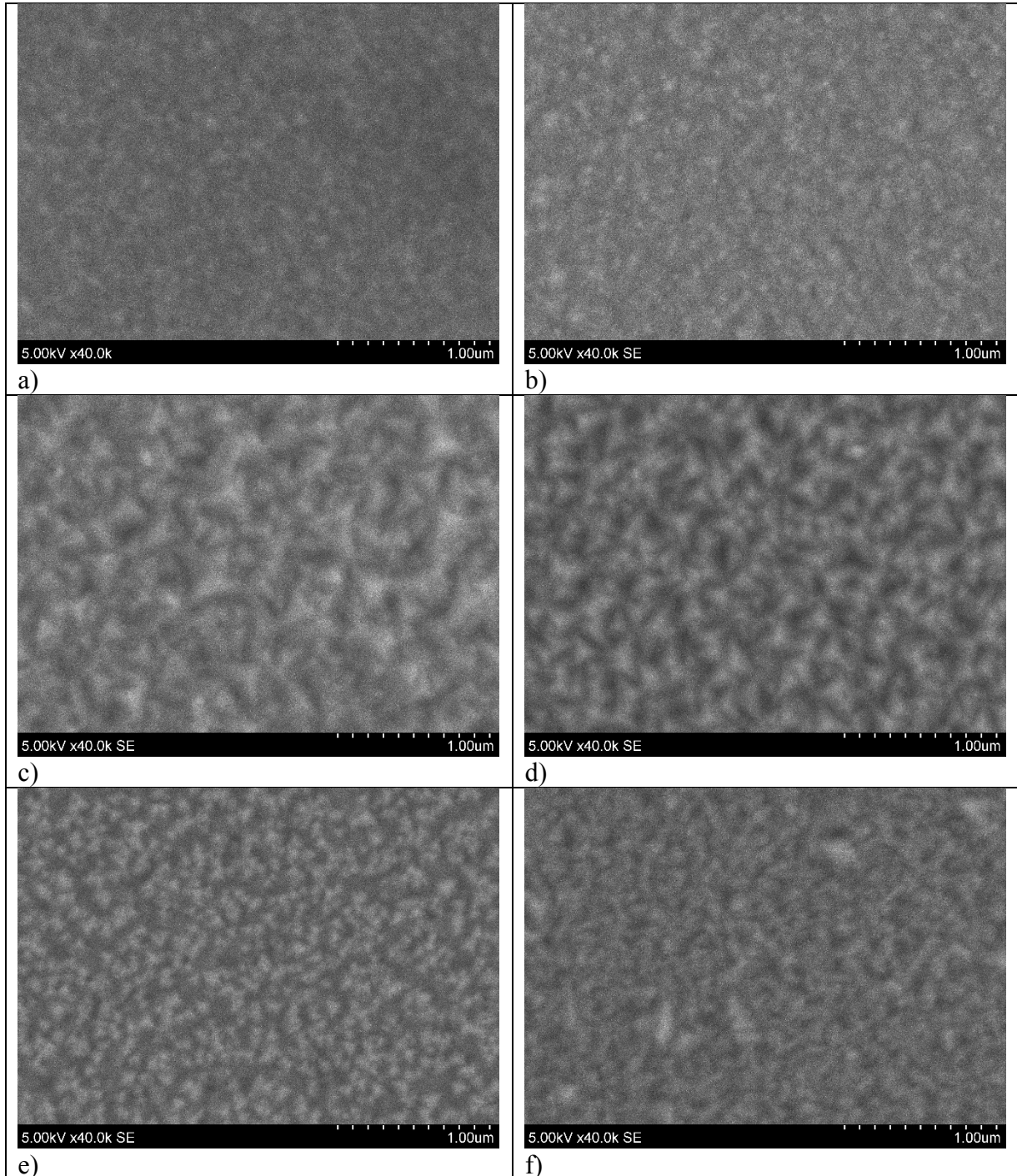**Fig. 3.2.1.** SEM picture of SDC thin ceramic films deposited on optical quartz substrates (SiO_2) using a) 0.2nm/s, 50°C b) 0.4nm/s, 450°C c) 0.8nm/s, 300°C d) 1.2nm/s, 450°C e) 0.8nm/s, 600°C f) 1.2nm/s, 600°C

In SEM analysis (Fig.3.2.1) it is difficult to detect which thin film coating is denser. Kinetically film growth depends on the parameters that determine their structural properties. But these structural properties influence conductivity. The overall process of the film formation can be divided into the following physical processes [46]:

(Steps of Thin Film Growth)

      1. Absorption (physisorption)

      2. Surface diffusion

      3. Chemical bond formation (chemisorption)

           – Molecule-molecule

           – Substrate-molecule

      4. Nucleation

      5. Microstructure formation

           – Crystal structure

           – Defects

      6. Bulk changes

           – Diffusion

           – Grain growth
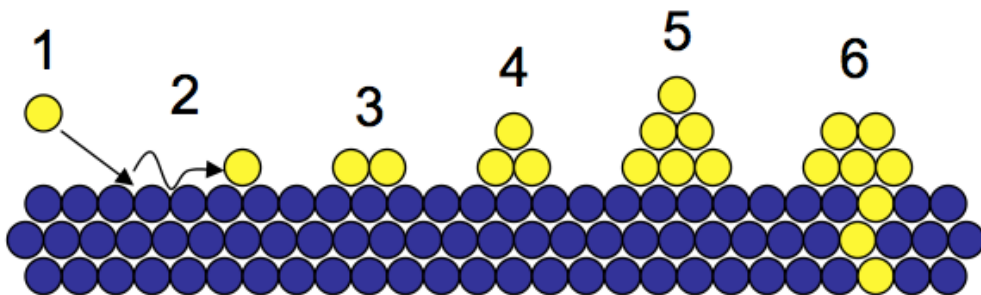
Fig. 3.2.2. The sequence of the film growth [46]

Thickness of deposited coating is one of the most important features in the study of thin coatings. A large number of surface conditions, and some parameters such as density of the obtained film depend on the coating thickness.

Depending on the temperature of the substrate, the grain size of the thin film changes as we see in Fig. 3.2.1. When the temperature of the substrates increases, the grain sizes increase, but this process occurs up to a certain temperature, in our case to 450 °C, and after that at a temperature of 600 °C, we notice a decrease in the grain size. This is due to the increased

influence of the growth rate at high temperatures. As we see in Fig. 3.2.1, all the thin films are uniform and do not have any defect or cracks.

3.3. EDS MEASUREMENTS

EDS measurements were carried out in order to establish homogeneity of obtained ceramic films. EDS investigations were performed for SDC20 on Alloy 600 substrates. In these investigations it is important to study the elemental composition of the film and the content of oxygen. EDS measurements were carried out at three different locations of each substrate.

Table 3.3.1. Elemental composition of SDC-TC thin films.

v_g, nm/s	T_{Sub}, °C	c_{Sm}, mol%	$<\Delta c_{Sm}>$, mol%	c_{Ce}, mol%	$<\Delta c_{Sm}>$, mol%	c_O, mol%	$<\Delta c_{Sm}>$, mol%
SDC_TC							
0.2	50	13.4	0.5	86.6	0.5	73.3	1.0
0.2	150	11.1	0.7	88.9	0.7	72.8	0.9
0.2	300	11.5	0.6	88.5	0.6	71.1	1.4
0.2	450	9.7	0.4	90.3	0.4	71.2	0.5
0.2	600	11.7	0.4	88.3	0.4	71.0	0.8
0.4	50	10.4	0.4	89.6	0.4	71.8	0.9
0.4	150	12.5	0.5	87.5	0.5	72.2	1.2
0.4	300	16.4	0.2	83.6	0.2	71.5	0.2
0.4	450	8.6	0.4	91.4	0.4	72.7	0.4
0.4	600	14.7	0.3	85.3	0.3	72.2	0.6
0.8	50	8.2	0.4	91.8	0.4	73.0	0.6
0.8	150	10.3	0.3	89.7	0.3	72.1	0.4
0.8	300	12.1	0.1	87.9	0.1	72.9	0.0
0.8	450	13.3	0.2	86.7	0.2	71.9	0.2
08	600	14.5	0.1	85.5	0.1	71.9	1.0
1.2	50	10.9	0.7	89.1	0.7	73.5	0.6
1.2	150	22.4	0.1	77.6	0.1	73.9	0.5
1.2	300	11.2	0.7	88.8	0.7	70.2	1.4
1.2	450	8.5	0.6	91.5	0.6	71.1	0.6
1.2	600	23.8	0.1	76.2	0.1	71.8	0.0
1.6	50	11.8	0.2	88.2	0.2	73.4	0.2
1.6	150	8.1	0.2	91.9	0.2	74.9	0.4
1.6	300	21.0	0.2	79.0	0.2	73.0	0.1
1.6	450	15.6	0.1	84.4	0.1	73.1	0.1
1,6	600	14.0	0.2	86.0	0.2	72.7	0.4

EDS measurements were carried out on SDC ceramic films at different deposition paramiters. In Table 3.3.1 (and) we calculated the concentration of the elemental composition of thin film not considering element composition of the substrate.

3.4. ANALISIS OF RAMAN SPECROSCOPY

Raman spectroscopy is a unique and universal method that can provide information about oxygen vacancies in the fluorite structure. Raman spectroscopy is an indestructible method and can provide information about the phase of the material, quality and purity. In our case, the Raman spectroscopy method was used to determine the parameters of thin films based on cerium oxide with samarium and gadolinium dopants obtained by electron beam evaporation in order to determine the effect of Sm and Gd coatings on the scattering.

In this paper, we attempt to explain the effect of the depositing parameter of thin films and substrates on the Raman spectra. As we mentioned earlier, thin films based on cerium oxide obtained at different deposition rates from 0.2 nm/s to 1.6 nm/s on different subgrades at various substrate temperatures.

Fig. 3.4.2 presents the Raman spectra of the thin film obtaned by e-beam deposition Ce_{1-x} Sm_x O_2 and Ce_{1-x} Gd_x O_2 powders, which can be confirmed by the fluorite phase with space group Fm3m shown in Fig. 3.1.1. Raman spectra for pure ceria were obtained by literature reviiew to confirm the formation of GDC and SDC and detect the Raman shift on these samples [53]. Main peak of pure ceria presents on $465cm^{-1}$ on F2g vibrational mode. In this mode can be move only oxygen atoms aroun the cerium ions Ce^{4+} [52, 53]. As we know in the fluorite lattic only oxygen atoms can be mobile, and the frequency of this mode should not depend on the mass of the cation [51].
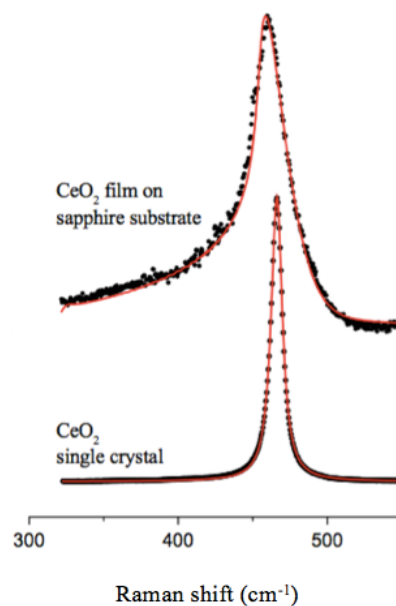

Fig. 3.4.1. Peak position of Raman spectra for pure ceria [53]

It is for this reason that the characteristics of the peaks are very sensitive to disorder induced in the oxygen ion sublattice of the oxide., in particular, the peak position and the width of the peaks [48, 52, 53]. With the doping of rare-earth Gd and Sm elements the crystal lattice of cerium, we get a defect in the crystal lattice that affected the environment of oxygen around the metal ions. As a result, we received Raman spectra, changes on the position of peaks and width of peaks.

Considering thin films of cerium oxide doped with Sm and Gd, it is seen that the F2g modes, in particular, first-order peaks inherent to cerium oxide, shifted to the region of lower wavenumbers (Fig. 3.4.2.). The Raman shift consists of -2 cm^{-1} to 5 cm^{-1} of a low-frequency wave. The peaks for all the samples were similar to each other in form but the wave numbers and their intensity varied depending on the studied sample.
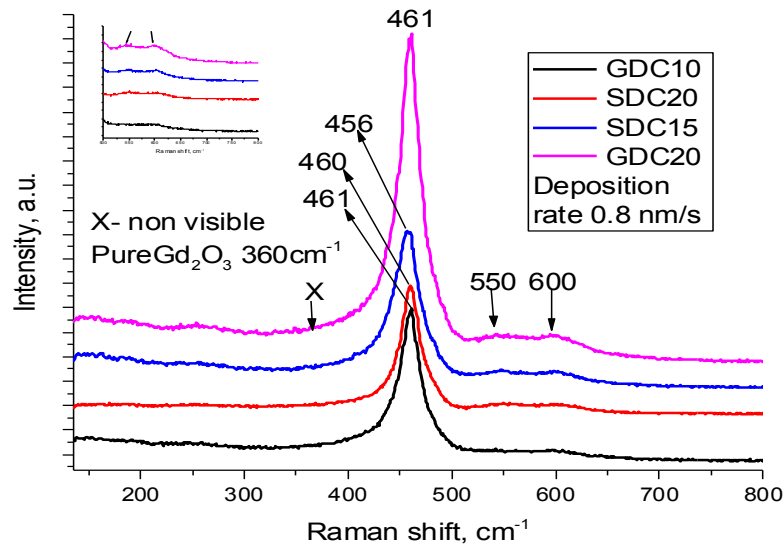

Fig. 3.4.2. Raman spectra of different composition of Gd and Sm doped ceria (GDC 10, GDC 20, SDC15 SDC 20) on Alloy600 substrate

In the Raman study peak positions are determined by fitting the data to the Lorentz line shape using a peak fit. As we can see in Fig. 3.4.2, the basic mode for GDC10 and GDC20 is at peak position 461cm^{-1}, and for SDC15 it is 456 cm^{-1} and for SDC20 the peak position are shown in 460cm^{-1}.

As the author [47] explains, the observed intense bands for doped cerium oxides are due to the Raman regime (F2g) of fluorite dioxide belonging to the space group (Fm3m). The shift of peak position to the region of lower wavenumbers shows that the F2g mode corresponds to the symmetric vibrations of oxygen ions around Ce^{4+} ions in octahedra CeO$_8$ [47 - 51].
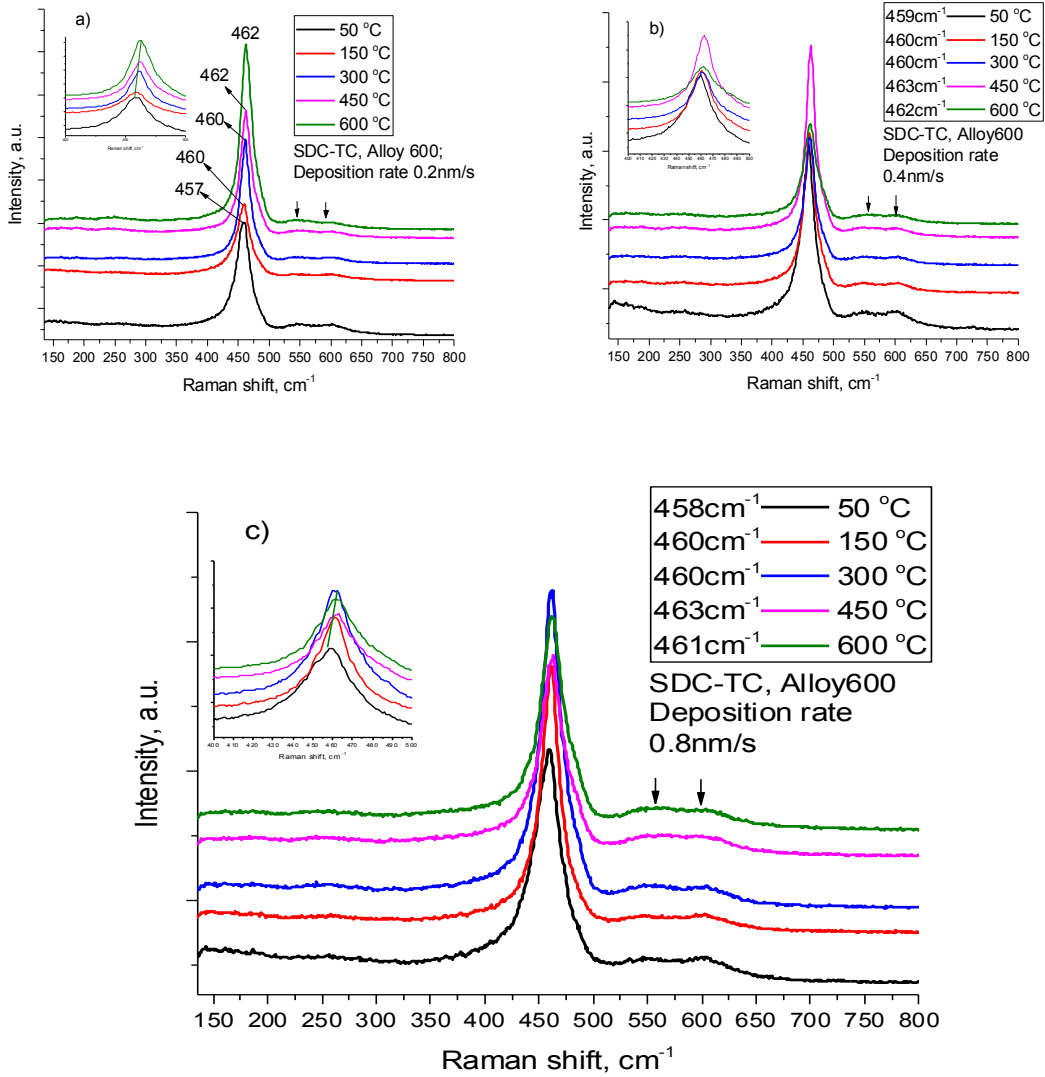
Fig. 3.4.3. Raman spectra of Sm doped ceria (SDC 20) on Alloy600 substrate at different temperatures from 50 ^{o}C to 600 ^{o}C and deposition rate: a) 0.2 nm/s, b) 0.4 nm/s, c) 0.8 nm/s

In Figs. 3.4.3 and 3.4.4 we can see the shift to a region of lower wavenumbers. The Raman shift to lower frequencies for the doped samples has two reasons: the first reason is an increase in oxygen vacancies caused by doping cerium oxide with rare-earth materials (it was described in the literature review) and the second reason, as the author [51, 54] points out, is the size factor i.e., the change in frequency $\Delta\omega$ associated with a change in the lattice constant Δa:

$$\Delta\omega = -3\gamma\omega_0\Delta a/a_0$$

$$(5)$$

where lattice Δa, ω_0 and a_0 are the Raman frequency and the lattice constant of CeO_2, respectively, $\gamma = 1.24$ is the Gruneisen parameter, the value of which was calculated in [51-54].
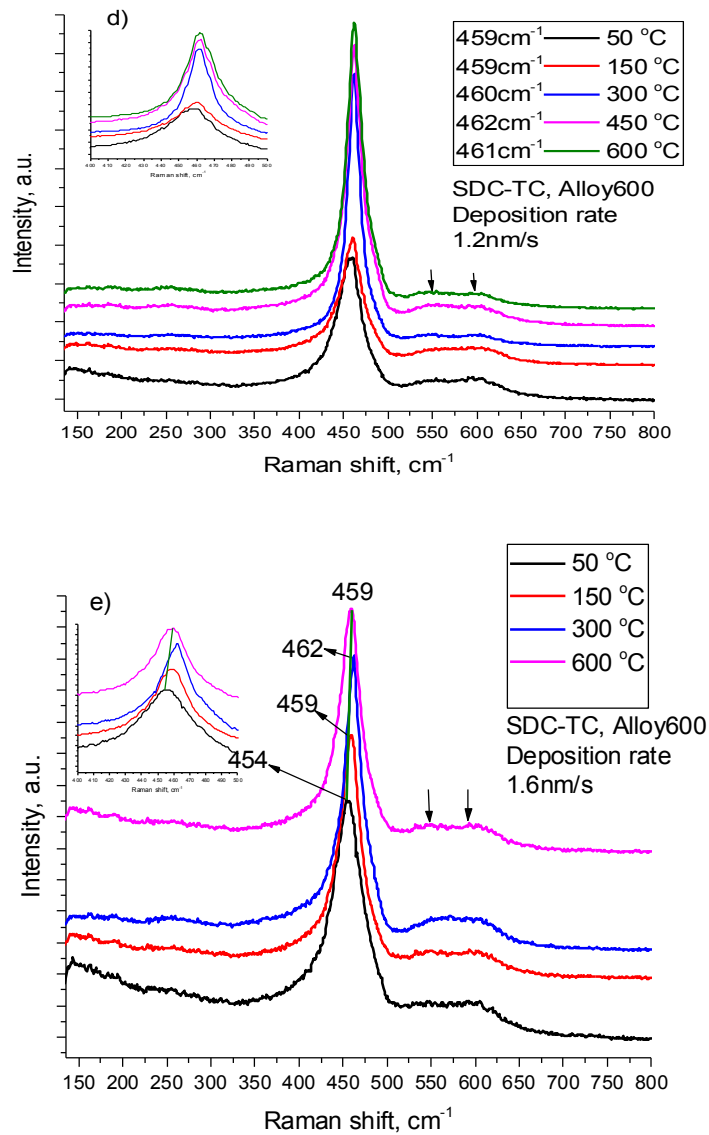

Fig. 3.4.4. Raman spectra of Sm doped ceria (SDC 20) on Alloy600 substrate at different temperatures from 50 $^{\circ}$C to 600 $^{\circ}$C and deposition rate: d) 1.2 nm/s, e) 1.6 nm/s
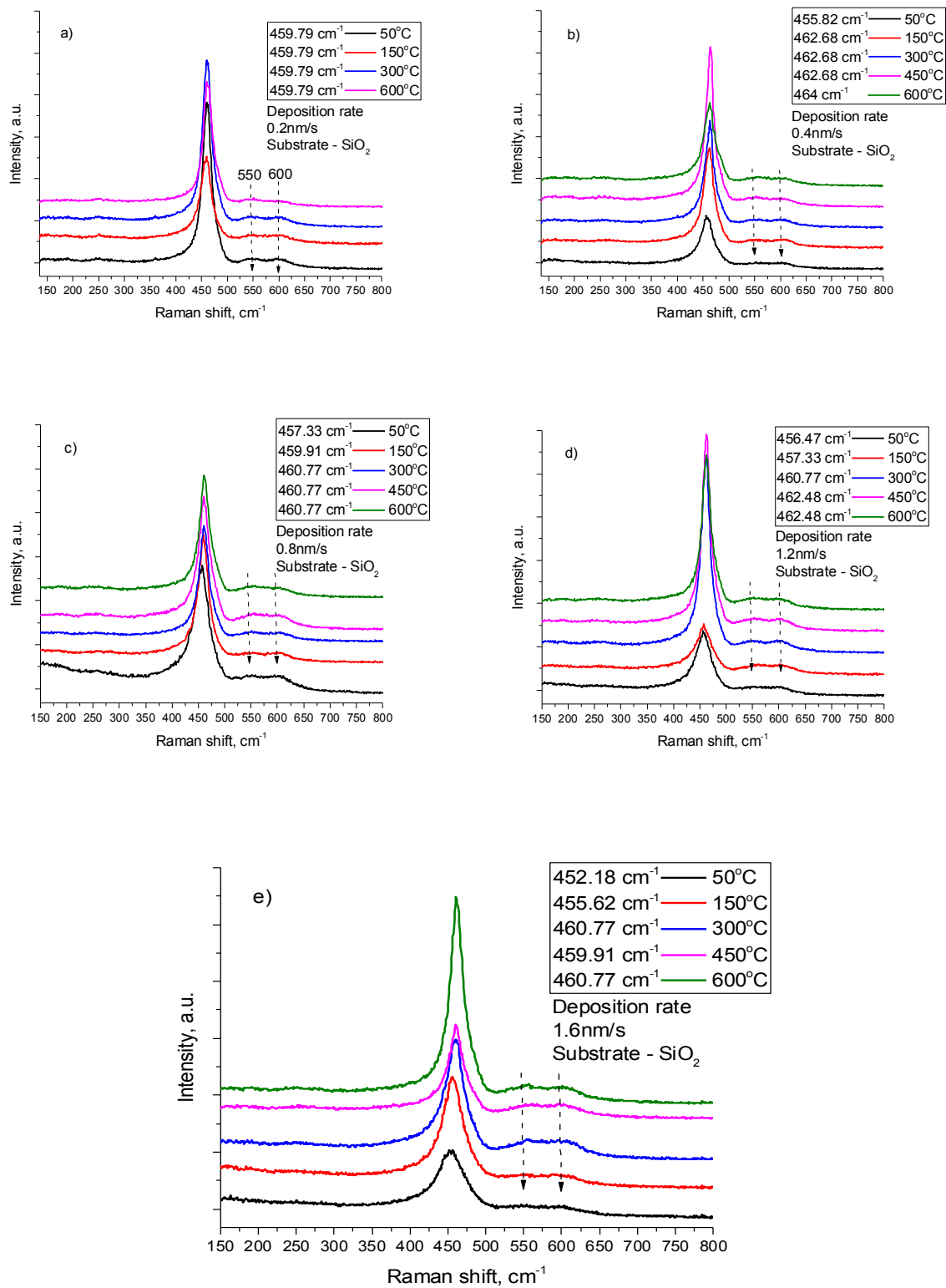
Fig. 3.4.5. Raman spectra of Sm doped ceria (SDC 20) on SiO_2 substrate at different temperature from 50 ^oC to 600 ^oC and depositiona rate: a) 0.2 nm/s, b) 0.4 nm/s, c) 0.8 nm/s d) 1.2 nm/s, e) 1.6 nm/s

In Fig. 3.4.5 we can see the shift to the region of lower wavenumbers. The Raman shift consists

of -1 cm^{-1} to 13 cm^{-1} of a low-frequency wave. The peaks for all the samples were similar to each other in a form. Peak position due to the F2g symmetry and shift in the F2g mode is explained by the change in M-O vibration friguency after the doping on rare-earth elements [57]. Thus, two broad additional peaks at 540- 550 and 600 cm^{-1} appear due to the presence of oxygen vacancies in all samples. As explained by the authors of many works [56, 57, 58] the paek position at 540 - 550 cm^{-1} corresponds to oxygen vacancies generated as charge compensation defects induced by the introduction of other metal cations into the crystal lattice of cerium. Peak position at 600 cm^{-1} it explained by non- stoichiometry oxygen vacancy in cerium oxide. For explain appearance of oxygen vacancy in Gd and Sm doped ceria is explained by the reaction:

$$\text{Oxygen vacancy model:} \qquad RE_2O_3 + 2CeO_2 \rightarrow 2RE'_{Ce} + 3V_O^x + V_{\ddot{O}} \qquad (6)$$

$$\text{Interstitial model:} \qquad Gd_2O_3 + 2CeO_2 \rightarrow 2Gd'_{Ce} + 3V_O^x + V_{\ddot{O}} \qquad (7)$$

$$Sm_2O_3 + 2CeO_2 \rightarrow 2Sm'_{Ce} + 3V_O^x + V_{\ddot{O}} \qquad (8)$$
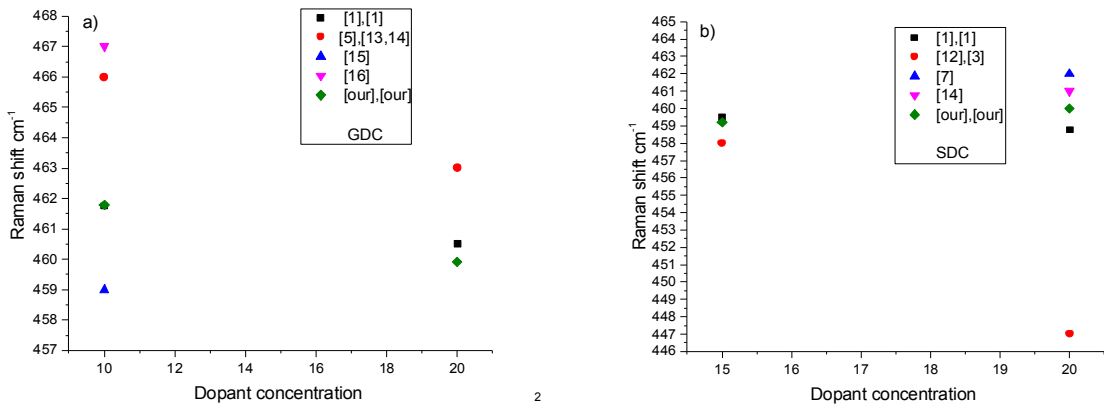

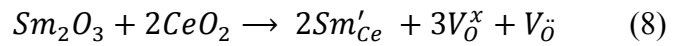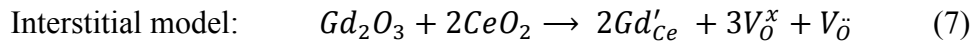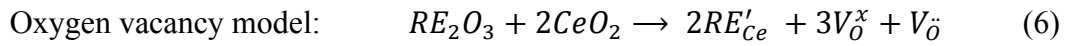**Fig. 3.4.6.** Raman shift of F2g mode versus dopant concentration (GDC 10, GDC 20, SDC15, SDC 20)
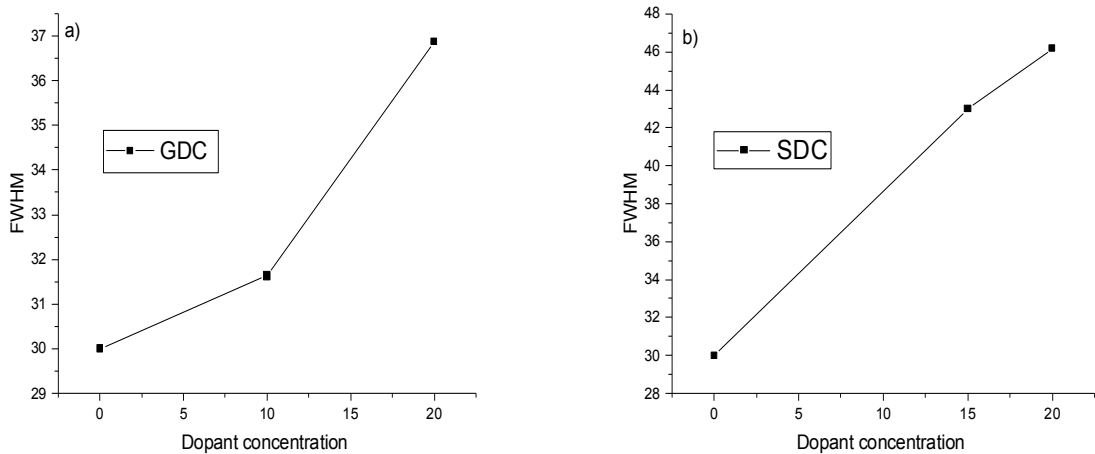
Fig. 3.4.7. FWHM of F2g mode versus dopamt concentration (GDC 10, GDC 20, SDC15 SDC 20)

Full width half maximum (FWHM). Raman shift of F2g mode on Gd and Sm doped ceria (Fig. 3.4.6 and 3.4.7). We see that in the case of SDC in Fig. 3.4.6. b) the dependence of Raman shift on dopant concentration. By increasing the dopant concentration the Raman spectra shifted to the lower frequency wave side. This dependence was obtained as a result of a comparison of the literature analysis [47, 50, 51, 5, 56, 57, 58, 59] and our results. This statement is more pronounced for the Sm doped ceari samples rather than Gd doped ceria, which is shown in Fig. 3.4.6. a).
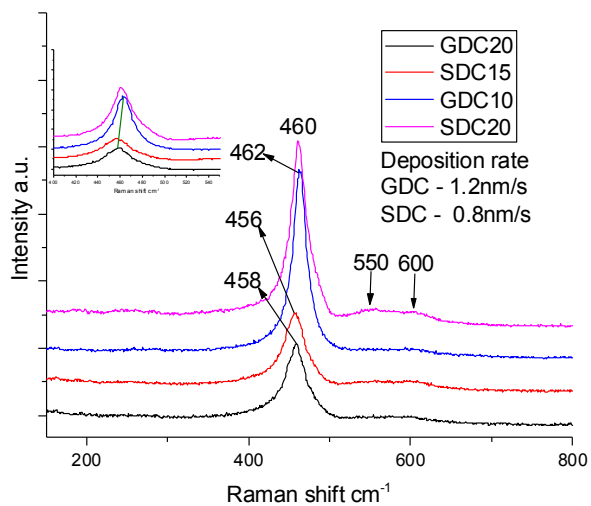

Fig. 3.4.8. Raman spectra of different composition of Gd and Sm doped ceria on SiO_2 substrate were deposition rate (GDC 10 and GDC 20) 1.2 nm/s, (SDC15 and SDC 20) 0.8 nm/s

FWHM in the F2g peaks are shown in Fig. 3.4.7 a) GDC, b) SDC) that fact by the

increasing of the dopant concentration Sm and Gd, the line of Raman peaks becomes wider and more asymmetric and it is visible in Fig. 3.4.8. As the author [60] showed, another reason for broadening and asymmetric shift of the Ramon peak is the presence of oxygen vacancies.

The dependence of oxygen stoichiometry on the particle size of nanocrystalline CeO_{2-x} is confirmed by the Raman spectroscopy data. The authors of [62, 63] noted that the Raman mode at 464 cm^{-1} is sensitive to a change in the oxygen stoichiometry of CeO_{2-x} due to size effects. The decrease in the size of the CeO_{2-x} nanoparticles leads to systematic changes in the Raman spectra, with the shift of the Raman peak to lower energies caused by an increase in the crystal cell parameter of CeO_{2-x}, and the broadening of the peak is determined by the inhomogeneous lattice tensions.
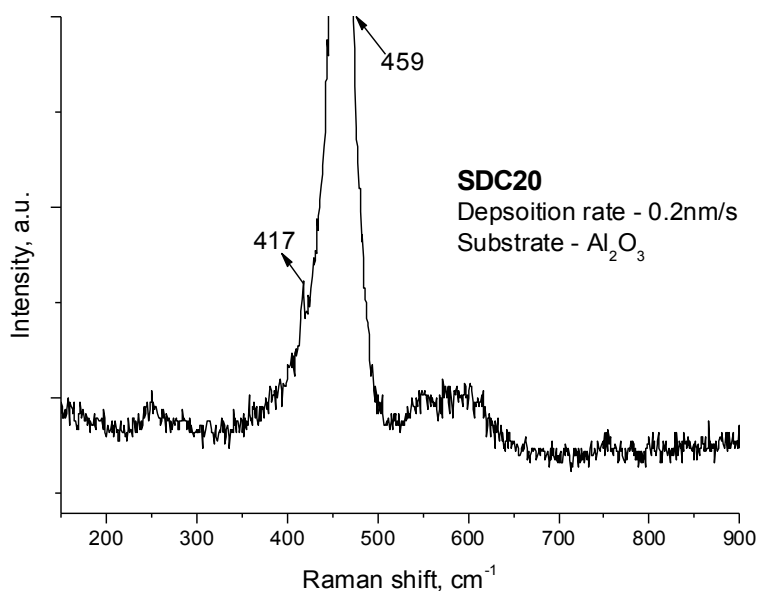
Fig. 3.4.9. Raman spectra of Sm doped ceria (SDC20) on Al_2O_3 substrate were deposition rate 0.2 nm/s

The observed pattern of changes in the cell size is caused by a gradual decrease in the effective degree of cerium oxidation due to the removal of part of the oxygen ions from the surface of the particles with the formation of oxygen vacancies. According to [61], the critical particle size at which the total Ce^{3+} - Ce^{4+} transition is observed is 1.9 nm. The proposed model of partial reduction of cerium includes protonation of surface oxygen atoms followed by removal of water and formation of oxygen vacancies.
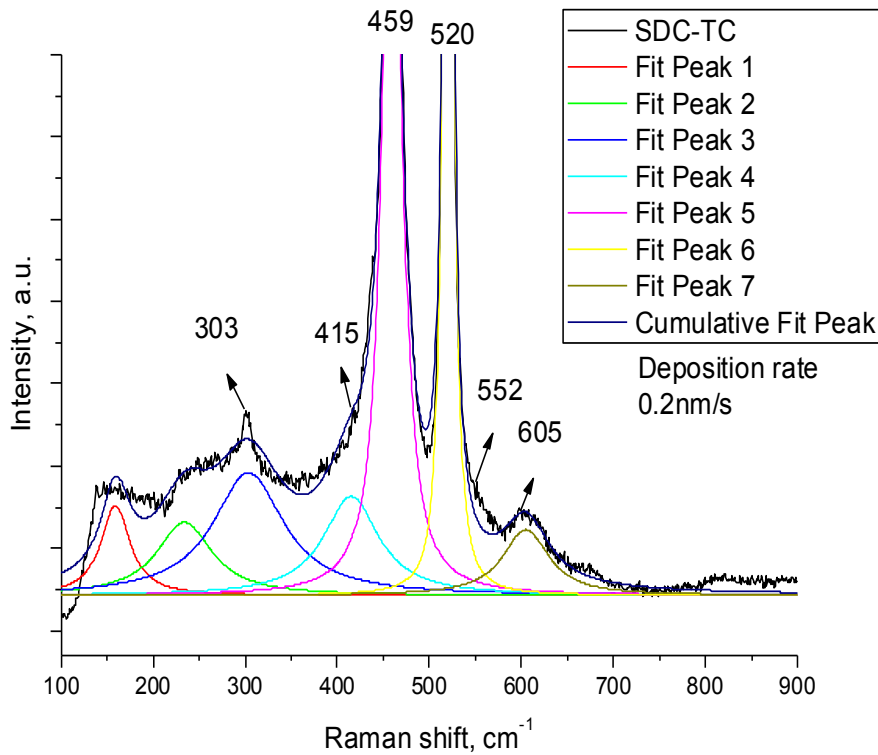
Fig. 3.4.10. Raman spectra of Sm doped ceria on Si (100) substrate were deposition

rate SDC 0.2 nm/s

Figs. 3.4.9 and 3.4.10 show that in Sm doped ceria on Al_2O_3 and Si (100) substrates with deposition rate 0.2 nm/s, Raman peaks have positions that are not expressed on other samples. Our results are in accordance with the reported data [49, 47, 50, 56], attributing these peaks at 303, 415 and 417 cm^{-1}, to Fg + Eg and Ag for samarium, respectively [49]. In addition, there was registered a peak position at 520 cm^{-1}, as we know from the literature this peak belongs to silicon, in our case this peak comes from the substrate. It is very important to note the fact that the vibrational mode corresponding to any free sesquioxide of rare-earth elements (Sm_2O_3, Gd_2O_3) does not show activity of the Raman peak phase expected at 360 cm^{-1}.

CONCLUSION

1. Thin films formed based on cerium oxide with (Gd and Sm) dopant retain crystalline structure of the initial evaporated powder, regardless of the concentration of the powder and used substrate.

2. SDC thin films have a single-phase and fluorite structure with space group Fm3m peaks corresponding to crystallographic orientations (111), (200), (220), (311), (222), and (400).

3. The crystallite size of formed SDC20 thin films increases with increasing temperature of the (Alloy 600 and SiO_2) substrates, the smallest crystallite size is d=6.8 nm when the temperature of substrate SiO_2 is $T_{sub} - 50^O C$ and d=7.5nm on Alloy 600 when $T_{sub} - 50^O C$).

4. SEM analysis shows that the susbtrate temperature has the influence on grain size of the formed thin films, i.e., the grain size increases till 450 °C substrate temperature and starts to decrease with further increase of the substarte temperature till 600 °C.

5. SDC and GDC thin ceramic films deposited on optical quartz substrates (SiO_2) at deposition rate from 0.2nm/s to 1.6 nm/s and the substrate temperature T_{sub}- from 50°C to 600°C are uniform and do not have defects or cracks.

6. The main Raman peak of pure ceria is presents at 465cm^{-1} and corresponds to the F2g vibrational mode, the Raman peak shifts 2 cm^{-1} for SDC15 and 5 cm^{-1} SDC20 thin films deposited on Alloy600 substrates. The peaks for all the samples were similar to each other in form, but the wave numbers and their intensity varied depending on the investigated sample.

7. The Raman peak (465cm^{-1} corresponding to pure ceria) shifts to the lower side from 1 cm^{-1} to 13 cm^{-1} for the formed (GDC10, GDC20, SDC15, SDC20) thin films. That could be influenced by an increase of oxygen vacancies and the size factor i.e., a change in frequency $\Delta\omega$ associated with a change in the lattice constant Δa.

8. SDC20 thin films formed on Al_2O_3 and Si (100) substrates with deposition rate of 0.2 nm/s, Raman peaks have positions that are not expressed on the other samples, attributing these peaks at 303, 415 and 417 cm^{-1}, these peak positions corresponded to Fg + Eg and Ag vibrational mode for samarium.

9. The most significant shift from 465cm^{-1} to 452 cm^{-1} is registered for Sm doped ceria (SDC 20) thin films deposited on SiO_2 (substrate temperature of T_{sub}- 50 ^{o}C and1.6 nm/s deposition rate) and the smallest shift from 465cm^{-1} to 464 cm^{-1} occurs for the peak related to the pure cerium when Sm doped ceria (SDC 20) thin films were deposited on SiO_2 with substrate temperature of T_{sub}- 600 ^{o}C and 0.4 nm/s deposition rate.

REFERENCES

1. www.intechopen.com/books/functionalized-nanomaterials/ Cerium Oxide Nanostructures and their Applications, March, 2017-03-18

2. http://www.doitpoms.ac.uk/tlplib/fuel-cells/Fig.s/YSZ-Nickel_sml.png Accessed 2015-10-16

3. 10 G. Brauer and K. A. Gingerich, J. Inorg. Nucl. Chem., 1960, 16, 87-99. 11

4. S. Vyas, Simulation of Ceria: Bulk and Surface Defects, University of London, 2005, pp. 85-143.

5. В.К. Иванов, А.Б. Щербаков, А.Е. Баранчиков, В.В. Козик НАНОКРИСТАЛЛИЧЕСКИЙ ДИОКСИД ЦЕРИЯ: свойства, получение, применение, 2013, pp. 107-274

6. https://amazingsolids.wordpress.com/2013/06/15 Imperfections in Solids –Stoichiometric and Impurity Defects April, 2017.03.23

7. J.W. Morris, Jr. Materials Science Defects in Crystals pp. 76-107

8. 2 A. Trovarelli, in Catalysis by Ceria and Related Materials, London, 2001, vol. 2, pp. 15-50.

9. Y. Zhou, N. J. Lawrence, L. Wang, L. Kong, T.-S. Wu, J. Liu, Y. Gao, J. R. Brewer, V. K. Lawrence, R. F. Sabirianov, Y.-L. Soo, X. C. Zeng, P. A. Dowben, W. N. Mei and C. L. Cheung, Angew. Chem. Int. Ed., 2013, 52, 6936-6939.

10. Y. Y. Zhou, N. J. Lawrence, T. S. Wu, J. Liu, P. Kent, Y. L. Soo and C. L. Cheung, Chemcatchem, 2014, 6, 2937-2946.

11. V. Grover, A.K. Tyagi. Phase relation studies in the CeO_2–Gd_2O_3–ZrO_2 system.// Journal of Solid State Chemistry 177 (2004) pp. 4197–4204.

12. O. Yamamoto, Low temperature electrolytes and catalysts, in: Handbook of Fuel Cells-Fundamentals, Technology and Application, Eds.: W. Vielstich et al., Vol. 4: Fuel Cell Technology and Applications, Wiley and Sons, Chichester, England (2003) p.1002

13. Taroco, H. A., Santos, J. A. F., Domingues, R. Z. and Matencio, T. Ceramic Materials for Solid Oxide Fuel Cells. http://intechopen.com/ p 423-445

14. S. M. Haile, Fuel cell materials and components.// Acta Materialia 51 (2003) pp. 5981–6000.

15. В.В. Сальников, Е.Ю. Пикалова, Изучение особенностей транспортных свойств электролитов на основе CeO_2 методами рамановской и импедансной спектроскопии, Физика твердого тела, 2015, том 57, вып. 10

16. T. Vinodkumar, Bolla Govinda Rao, Benjaram M. Reddy, Influence of isovalent and aliovalent dopants on the reactivity of cerium oxide for catalytic applications, Catalysis Today 253 (2015) p 57–64.

17. Kosacki I., Suzuki T., Anderson H.U., Colomban P. Raman scattering and lattice defects in nanocrystalline CeO_2thin films // Solid State Ionics. 2002. Vol. 149. P. 99-105.

18. Kosacki I., Petrovsky V., Anderson H.U. Raman spectroscopy of nanocrystalline ceria and zirconia thin films // J. Am. Ceram. Soc. 2002. Vol. 85. P. 2646-2650.

19. Spanier J.E., Robinson R.D., Zhang F. et al. Size-dependent properties of CeO_2-y nano-particles as studied by Raman scattering // Phys. Rev. B. 2001. Vol. 64. P. 245407.

20. Jessica T. Dahle, Yuji Arai 2. Environmental Geochemistry of Cerium: Applications and Toxicology of Cerium Oxide Nanoparticles//Int. J. Environ. Res. Public Health 2015, 12, 1253-1278; doi:10.3390/ijerph120201253.

21. Migani A., Vayssilov G.N., Bromley S.T. et al. Dramatic reduction of the oxygen vacancy formation energy in ceria particles: a possible key to their remarkable reactivity at the nanoscale // J. Mater. Chem. 2010. Vol. 20. P. 10535-10546.

22. O'Hayre, R. Fuel Cell Fundamentals 2nd Edition / R. O'Hayre, S.-W. Cha, W. Colella, F.B. Prinz. - Hoboken:Wiley, 2009. – P. 576.

23. Duprez D., Descorne C., Birchem T., Rohart E. Oxygen storage and mobility on model three-way catalysts // Topics Catal. 2001. Vol. 16(1-4). P. 49-56.

24. Adnan Younis, Dewei Chu, Sean Li. Cerium Oxide Nanostructures and their Applications// ISBN 978-953-51-2855-7, Published: December 28, 2016

25. N. Minh, T. Takahashi, Science and Technology of Ceramic Fuel Cells, Chapter 3, Electrical Conduction in Ceramics, 1995, pp. 41-68

26. Martorana, F. Giannici, A. Longo, Synchrotron Radiation: Basics, Methods and Applications, Springer, 2015, Chapter 27, Synchrotron Radiation and Chemistry - Studies of Materials for Renewable Energy Sources; pp. 697-715

27. A. Boudghene Stambouli 1, E. Traversa Solid oxide fuel cells (SOFCs): a review of an environmentally clean and efficient source of energy, Renewable and Sustainable Energy Reviews 6 (2002) 433–455

28. Fuel cell materials by Nextech materials. August 2001. http://www.fuelcellmaterials.com/site/powders-and-pastes/electrolytes

29. Katherine Develos- Bagarinao.Nanostructured Cerium Oxide Films: Synthesis, Properties and Applications// DOI 10.1007/978-3-319-14478-8-11

30. Борисенко А.И. В.В. Новиков, Н.Е. Приходько, М.М. Митникова, Л.Ф. Чепик.– Л. Тонкие неорганические пленки в микроэлектронике/ Наука, 1972. – 114 с.

31. Максимчук Н.В. Свойства и практическое применение нанокристаллических пленок оксида церия / Н.В. Максимчук, А.Н. Шмырева, А.В. Борисов // Технология и конструирование в электронной аппаратуре. – 2010. – № 5. – 6. – С. 54–59

32. Metallic Mirror Coatings// https://www.edmundoptics.com/resources/application-notes/optics/metallic-mirror-coatings/ April 29. 2017

33. S. Seghaier, N. Kamoun, R. Brini, A.B. Amara. Structural and optical properties of PbS thin films deposited by chemical bath deposition/ Materials Chemistry and Physics 97 (2006) 71–80

34. S. N. AGBO, P. SUTTA. PREFERRED CRYSTAL ORIENTATION IN THIN-FILM NANOCRYSTALLINE SILICON DETERMINED BY RAMAN SPECTROSCOPY // Vol. 8, No. 4, October- December 2013, p. 1461 – 1473

35. Химические методы получения тонких пленок/ Н.В. Суйковская – Л.: Химия, 1971. – 230 с.

36. Л.В. Трушникова, В.В. Соколов, В.В. Баковец, Ю.И. Веснин, Т.Д. Пивоваров // сборник второй всероссийская конференция по наноматериалам «НАНО 2007». – Новосибирск.: изд-во НГУ, 2007 – С. 248

37. Х.О. Сергеевна. Технология получения оксидных систем CeO_2–SiO_2 и CeO_2– SnO_2 в тонкопленочном и дисперсном состояниях из пленкообразующих растворов и их свойства// 14 May, 2017

38. Мошнико В.А Теруков Е.И, Основы водородной энергетики СПбГЭУТУ "ЛЭТИ" , 2010.288p

39. Mehta, V. Review and analysis of PEM fuel cell design and manufacturing / V. Mehta, J.S. Cooper // J. Power Sources – 2003. – Vol. 114. – № 1. – P. 32–53.

40. Prashant Goura, Ranjit Nikose, Application of Fuel Cell in Power Plant to Reduce the Carbon-dioxide Emission ,(IJCEM) Volume 1, Issue 5, August 2014.

41. John Wiley and Sons, Progress in Solid oxide fuel cells, The American Ceramic Society.2010.p531

42. Marcia Zalbowitz Sharon Thomas. Fuel cells - green power. Los Alamos National Laboratory, 1:24, 1999

43. А.Иванов, Б.Смирнов, Электронно-лучевое напыление, http://www.nanoindustry.su/, 22 April ,28-34 p.

44. PVD 75,Thin film deposition system operation manual PVD 75,Kurt J. Lesker Company, http://www.physics.umu.se/ 23 April, 242 p.

45. Rachel Oommen1, Usha Rajalakshmi1 and Sanjeeviraja2, Characteristics of Electron Beam Evaporated and Electrodeposited Cu2O thin films – Comparative study, International Journal of ELECTROCHEMICAL SCIENCE, http://www.electrochemsci.org/ 25 April, (8289-8297 p.).

46. Thin Film Growth and Evolution, http://crysta.physik.hu-berlin.de/28 April, 37 p.

47. S.A. Acharya, V.M. Gaikwad, S.W. D'Souza, S.R. Barman. Gd/Sm dopant-modified oxidation state and defect generation in nano-ceria// Solid State Ionics 260 (2014) 21–29

48. E.C.C. Souzaa, H.F. Britob, E.N.S. Muccilloa. Optical and electrical characterization of samaria-doped ceria// Journal of Alloys and Compounds 491 (2010) 460–464

49. V. Laira, L.S. Zˇivkovic, O. Lupana, A. Ringuedéa. Synthesis and characterization of electrodeposited samaria and samaria-doped ceria thin films// Electrochimica Acta 56 (2011) 4638–4644

50. Yu-Lin Kuo, Yu-Ming Su, Jia-Yu Chang. A facile method for the deposition of Gd_2O_3-doped ceria films by atmospheric pressure plasma jet // Thin Solid Films 570 (2014) 215–220

51. В.В. Сальников, Е.Ю. Пикалова. Изучение особенностей транспортных свойств электролитов на основе CeO_2 методами рамановской и импедансной спектроскопии// Физика твердого тела, 2015, том 57, вып. 10

52. T. Vinodkumar, Bolla Govinda Rao, Benjaram M. Reddy. Influence of isovalent and aliovalent dopants on the reactivity of cerium oxide for catalytic applications// Catalysis Today 253 (2015) 57–64

53. I. Kosacki, T. Suzuki, V. Petrovsky, H.U. Anderson and Ph. Colomban, Raman Scattering and Lattice Defects in Nanocrystalline CeO_2 Thin Films, Solid State Ionics 149 (1-2) (2002) 99.

54. T. Sato and S. Tateyama, Phys. Rev. B: Condens. Matter **26**, 2257 (1982).

55. Yu-Chuan Wu, Ming-Jin Lee, Xiang Li. Analysis of the microstructure and physical properties of $La_{0.85}Sr_{0.15}Ga_{0.8}Mg_{0.2}O_{2.825}$ and $Ce_{0.85}Sm_{0.15}O_{1.925}$ composite electrolytes used in solid oxide fuel cells// Journal of the European Ceramic Society 35 (2015) 4485–4495

56. K.C. Anjaneya, G.P. Nayaka, J. Manjanna, G. Govindaraj, K.N. Ganesha. Preparation and characterization of $Ce_{1-x}Gd_xO_{2-d}$ (x = 0.1–0.3) as solid electrolyte for intermediate temperature SOFC// Journal of Alloys and Compounds 578 (2013) 53–59

57. K.C. Anjaneya, G.P. Nayaka, J. Manjanna, G. Govindaraj, K.N. Ganesha. Studies on structural, morphological and electrical properties of $Ce_{0.8}Ln_{0.2}O_{2-d}$ (Ln = Y^{3+}, Gd^{3+}, Sm^{3+}, Nd^{3+} and La^{3+}) solid solutions prepared by citrate complexation method// Journal of Alloys and Compounds 585 (2014) 594–601

58. Nityanand Chaubey, B.N. Wani, S.R. Bharadwaj, M.C. Chattopadhyaya. Physicochemical properties of rare earth doped ceria $Ce_{0.9}Ln_{0.1}O_{1.95}$ (Ln 1⁄4 Nd, Sm, Gd) as an electrolyte material for IT-SOFC/SOEC// Solid State Sciences 20 (2013) 135e141

59. L.D. Jadhav, M.G. Chourashiya, A.P. Jamale, A.U. Chavan, S.P. Patil. Synthesis and characterization of nano-crystalline $Ce_{1-x}Gd_xO_{2-x/2}$ (x = 0–0.30) solid solutions// Journal of Alloys and Compounds 506 (2010) 739–744

60. J.E. Spanier, R.D. Robinson, F. Zhang, S.W. Chan, I.P. Herman, Phys. Rev. B 64 (2001) 245407.

61. Structural study on monosize CeO_{2-x} nano-particles / S. Tsunekawa, R. Sivamohan, S. Ito [et al.] // Nanostruct. Mater. – 1999. – V.11. – P.141-147.

62. Empirical-method for determining CeO_2-particle size in catalysts by raman- spectroscopy / G.W. Graham, W.H. Weber, C.R. Peters, R. Usmen // J. Catalysis. – 1991. – V.130. – P.310-313.

63. Weber W.H. Raman-study of CeO_2 2nd-order scattering, lattice-dynamics and particle-size effects / W.H. Weber, K.C. Hass, J.R. McBride // Phys. Rev. B. – 1993. – V.48. – P.178-185.